

Dynamics of a Data-Driven Low-Dimensional Model of Turbulent Minimal Pipe Flow

C. Ricardo Constante-Amores^{1,2†}, Alec J. Linot³, Michael D. Graham¹

¹Department of Chemical and Biological Engineering, University of Wisconsin-Madison, Madison WI 53706, USA

²Department of Mechanical Science and Engineering, University of Illinois, Urbana Champaign, IL 61801, USA

³Department of Mechanical and Aerospace Engineering, University of California, Los Angeles, CA 90095, USA

The simulation of turbulent flow requires many degrees of freedom to resolve all the relevant times and length scales. However, due to the dissipative nature of the Navier-Stokes equations, the long-term dynamics are expected to lie on a finite-dimensional invariant manifold with fewer degrees of freedom. In this study, we build low-dimensional data-driven models of pressure-driven flow through a circular pipe. We impose the ‘shift-and-reflect’ symmetry to study the system in a minimal computational cell (e.g., smallest domain size that sustains turbulence) at a Reynolds number of 2500. We build these models by using autoencoders to parametrize the manifold coordinates and neural ODEs to describe their time evolution. Direct numerical simulations (DNS) typically require on the order of $\mathcal{O}(10^5)$ degrees of freedom, while our data-driven framework enables the construction of models with fewer than 20 degrees of freedom. Remarkably, these reduced order models effectively capture crucial features of the flow, including the streak breakdown. In short-time tracking, these models accurately track the true trajectory for one Lyapunov time, while at long-times, they successfully capture key aspects of the dynamics such as Reynolds stresses and energy balance. Additionally, we report a library of exact coherent states (ECS) found in the DNS with the aid of these low-dimensional models. This approach leads to the discovery of seventeen previously unknown solutions within the turbulent pipe flow system, notably featuring relative periodic orbits characterized by the longest reported periods for such flow conditions.

1. Introduction

The prevalence of wall turbulence in a diverse range of industrial and everyday applications has attracted substantial interest, as approximately 25% of the energy consumed by industry is dedicated to transporting fluids through pipes and channels, and about one-quarter of this energy is dissipated due to turbulence occurring near walls (Jiménez & Moin 1991; Jiménez 2013; Avila *et al.* 2023). Pipe flow has been the subject of extensive research since the groundbreaking experiments conducted by Reynolds nearly two centuries ago (Reynolds 1883). The dynamics of flow are solely governed by the Reynolds number, which characterizes the ratio of inertial forces to viscous forces. The transition of pipe flow from laminar to turbulent, and the behavior beyond this critical point have resulted in numerous comprehensive reviews (see e.g. Mullin (2011); Eckhardt *et al.* (2007); Smits *et al.* (2011); Avila *et al.* (2023)).

† Email address for correspondence: crconsta@illinois.edu

Plane Couette and pipe flow are two canonical configurations as they provide a simplified setting to explore fundamental mechanisms of wall-bounded turbulence (Pope 2000). Plane Couette flow is easier to compute numerically but proves challenging to replicate experimentally due to the intricate requirements of moving sidewalls in opposite directions (Nagata 1990). On the other hand, pipe simulations are less prevalent due to the necessity of cylindrical coordinates and the inherent geometrical singularity at the pipe axis. Pioneering simulations conducted by Eggels *et al.* (1994) offered initial insights into the rich dynamics up to a friction Reynolds number of approximately $Re_\tau \approx 180$. These investigations were subsequently expanded upon by studies conducted at higher Reynolds numbers by El Khoury *et al.* (2013) and Ahn *et al.* (2015). With the increase in computational power, the most recent Direct Numerical Simulations (DNS) in turbulent pipe flow have achieved friction Reynolds numbers of approximately $Re_\tau \approx 5200$ (Lee & Moser 2015), $Re_\tau \approx 6000$ (Pirozzoli *et al.* 2021) and $Re_\tau \approx 12000$ (Pirozzoli 2024).

The focus of the present work is the extent to which modern data-driven methods can capture the nonlinear dynamics of turbulent pipe flows near transition. The critical Reynolds value for transition may vary from 1700 to 2300, and even values above 3000 have been reported (Darbyshire & Mullin 1995; Eckhardt 2007; Faisst & Eckhardt 2004). Because of its geometric and dynamical simplicity, the ‘minimal flow unit’ (MFU) of pipe flow has been previously presented (Willis *et al.* 2013, 2016; Budanur *et al.* 2017; Kaszás & Haller 2024; Constante-Amores & Graham 2024). The MFU represents the smallest domain size capable of sustaining turbulence, described by Jiménez & Moin (1991) in the context of plane Couette flow. It encapsulates the essential elements of turbulent dynamics, particularly the ‘self-sustaining process’ (SSP) described by (Hamilton *et al.* 1995). In this process, low-speed streaks near the wall become unstable and wavy, leading to their breakdown and the formation of rolls. These rolls then lift fluid from the walls, thereby regenerating the streaks and perpetuating the cycle. Given that the state space dimension (number of mesh points times number of velocity components) for fully resolved direct numerical simulation (DNS) even for the MFU case are beyond $\mathcal{O}(10^5)$ (Willis *et al.* 2013; Budanur *et al.* 2017), efforts have been made to build reduced models. Willis & Kerswell (2009) proposed the $2 + \epsilon$ dimensional model that captures structures observed in the fully nonlinear dynamics of 3D DNS pipe flow.

To understand the intricate nonlinear dynamics of turbulence, researchers have adopted a dynamical systems perspective. The turbulent nonlinear dynamics of fluids are governed by the (infinite-dimensional) Navier-Stokes equations (NSE). Despite this infinite-dimensionality, the long-time dynamics are expected to lie on a finite-dimensional invariant manifold within state space (we discuss this point in more detail below). From this viewpoint, turbulence can be seen as a chaotic attractor of the NSE. Turbulent flows display persistent patterns in space and time, commonly known as exact coherent states (ECS) (Kawahara *et al.* 2012; Graham & Floryan 2021). There are several ECS types: steady or equilibrium solutions, periodic orbits, travelling waves, and relative periodic orbits. It has been proposed that the turbulent attractor can be decomposed into a collection of such ECS and by modelling the time spent by solutions near each ECS and transitions between them, the long-time statistics of the turbulent attractor can be predicted (Budanur *et al.* 2017; Page *et al.* 2024). In wall-bounded turbulence, the earliest studies on ECS have focused on plane Couette flow. Nagata (1990) found the first ECS, which were fixed-point solutions. Waleffe (1998) later connected ECS from plane Couette flow and plane Poiseuille flow to the SSP. However, fixed-point ECS cannot capture the dynamics entirely; periodic orbits can represent key aspects of nonlinear turbulent dynamics, such as bursting behavior. Based on this, Kawahara & Kida (2001) discovered the first two periodic orbits for MFU plane Couette flow, one of which resulted

in statistics that agreed well with the SSP. In the realm of pipe flow, early studies focused on ECS and their role in the transition to turbulence (Faisst & Eckhardt 2003; Wedin & Kerswell 2004; Pringle & Kerswell 2007; Pringle *et al.* 2009; Duguet *et al.* 2008; Willis & Kerswell 2008; Viswanath & Cvitanović 2009). The first set of ECS discovered, presented by Faisst & Eckhardt (2003); Wedin & Kerswell (2004), were traveling-wave solutions, which were also observed in experimental turbulent pipe flow settings (Hof *et al.* 2004; de Lozar *et al.* 2012). To date, several studies in pipe flow have focused on the discovery and classification of ECS according to the value of their dissipation, wave speed, and spatial symmetry (Pringle *et al.* 2009; Willis *et al.* 2013; Budanur *et al.* 2017). Willis *et al.* (2013) and Willis *et al.* (2016) reported 29 solutions, visualized new ECS in state space by symmetry reduction, showing the connections of relative periodic orbits with the turbulent attractor. Budanur *et al.* (2017) reported new ECS: 49 relative periodic orbits and 10 traveling waves. The results from Budanur *et al.* (2017) further supported the idea that turbulence wanders around ECS.

However, identifying ECS presents a challenge due to the high dimensionality of the state space. To find ECS, we can use methods based on traditional Newton-Raphson methods or more advanced techniques such as Jacobian-Free Newton-Krylov, where the Jacobian is not implicitly calculated (Willis 2019). Hence, it is imperative to commence from relatively favorable initial conditions to ensure the method's success due to several factors: the high dimensionality of the systems; the nonlinearity of the NSE; and the optimization landscape associated with finding ECS is often nonconvex, containing many local minima and saddle points (e.g., Newton-based methods tend to converge to local minima). Favorable initial conditions help narrow the search area and increase the likelihood of finding ECS. Parker & Schneider (2022) proposed the idea of using variational methods to find unstable periodic orbits for Kolmogorov flow, demonstrating that their method can converge to more solutions than a shooting method. Page & Kerswell (2020) introduced the idea of using dynamic mode decomposition to find unstable periodic orbits, particularly in cases where near recurrence is unlikely. Linot & Graham (2023) discovered new ECS in plane Couette flow by using converged ECS from low-dimensional models as initial conditions for the DNS, potentially revealing previously unknown ECS (e.g., in this work we will follow this approach). Additionally, finding ECS at large Reynolds numbers is still very challenging (recently Page *et al.* (2024) used automatic differentiation for finding ECS in relative large values of Reynolds numbers for 2D Kolmogorov flow). This limitation has resulted in the focus on identifying ECS at Reynolds numbers near the transition region to turbulence.

Developing reduced order models helps us to better understand the fundamental physics. These models can then be used to create effective control strategies (Linot *et al.* 2023b). In recent years, there has been a surge in the application of data-driven methodologies to gain insights into the intricacies of the transition to turbulence. While some of these approaches, such as the dynamic mode decomposition (Schmid 2010), and connected to the Koopman operator by (Rowley *et al.* 2009), offer linear perspectives, they encounter challenges in predicting heteroclinic connections for plane Couette flow, as highlighted by Page & Kerswell (2019). Recognizing the limitations of linear techniques, there has been a notable shift towards nonlinear methods. In particular, invariant-manifold-based approaches (and discussed in the following paragraphs). Another nonlinear framework gaining importance is spectral submanifolds methods (SSM), which facilitate the construction of invariant manifolds near known stationary points (Li *et al.* 2022; Kaszás & Haller 2024). Kaszás & Haller (2024) employed SSM to successfully identify the invariant manifold delineating the edge of chaos in pipe flow. This manifold serves as a crucial boundary, demarcating the transition from the laminar state to

turbulence within the phase space of the NSE. We note that SSM hat they must be ‘anchored’ to a known stationary point, while the framework that we use here, it does not need this requirement.

The accurate simulation of MFU pipe flow requires a large state space to resolve all the relevant spatial and temporal scales. For example, Willis *et al.* (2013) and Budanur *et al.* (2017) require on the order of $\mathcal{O}(10^5)$ degree of freedom to capture the complex nonlinear turbulent dynamics. Performing data-driven modeling in the full state space is computationally challenging. But, due to the dissipative nature of the NSE, it is expected that viscosity attenuates the high wave numbers; as a result, the long-term dynamics are confined to an invariant manifold with fewer degrees of freedom than the full state dimension (Temam 1989; Zelik 2022). The right dimension of this invariant manifold is not known beforehand, and it must be estimated from data. The most common method for linear dimension reduction is principal component analysis (PCA, also known as Proper Orthogonal Decomposition, POD, in the fluid dynamics community), which is based on the idea of the projection of the state onto the set of orthogonal modes that capture the maximum energy of the data (Jolliffe 1986; Abdi & Williams 2010; Holmes *et al.* 2012). However, PCA predicts a flat manifold because it is an inherently linear technique, which is a bad approximation for complex nonlinear problems. Thus, nonlinear techniques for dimension reduction have emerged such as autoencoders. Autoencoders consist of a pair of neural networks in which one network maps from a high-dimensional space to a low-dimensional space, and the other maps back (Kramer 1991; Hinton & Salakhutdinov 2006; Milano & Koumoutsakos 2002). For very high-dimensional systems, it can be advantageous to perform an initial linear dimension reduction step with PCA, followed by further nonlinear dimension reduction using an autoencoder (Linot & Graham 2023; Young *et al.* 2023; Constante-Amores *et al.* 2024a). Additionally, applying PCA and an autoencoder in parallel can be beneficial, as it allows for learning a low-dimensional nonlinear representation that corrects the linear representation (Linot & Graham 2020). Recently, Jing *et al.* (2020) developed a modified autoencoder for learning low-rank representations in image-based classification. This technique was subsequently adapted for dynamical systems data by Zeng *et al.* (2024), demonstrating that the architecture can produce robust and accurate estimates of the data manifold, and generate an orthogonal manifold coordinate system.

Once we have a low-dimensional representation of the full-state, we can proceed in data-driven modelling of the dynamics in manifold coordinates. Two different approaches can be done, either a function-space approach (in which the manifold coordinates are light to a higher-dimensional space of observables where the dynamics behave linear (e.g., see Otto & Rowley (2019); Constante-Amores *et al.* (2024a); Constante-Amores & Graham (2024); Constante-Amores *et al.* (2024b)) or a state-space approach (in which an evolution equation is learned in manifold coordinates). In this work, we apply the latter. A state space approach has been applied to chaotic problems including the 1D Kuramoto-Sivashinsky equation (Linot & Graham 2020; Liu *et al.* 2024), 2D Kolmogorov flow (Pérez-De-Jesús & Graham 2023), Couette flow (Linot & Graham 2023; Kaszás *et al.* 2022). Linot & Graham (2020) presented the framework known as DManD which stands for ‘data-driven manifold dynamics’ (DManD). In DManD, an autoencoder finds a low-dimensional representation of the full-state, and then a neural ODE (NODE) learns an evolution equation of this low-dimensional representation. NODE is based on the idea that a neural network parameterises the derivative of the vector field of the latent space (Chen *et al.* 2019; Linot & Graham 2022). DManD models applied to chaotic systems are capable of faithfully capturing the short- and long-time statistics of the system with a small number of degrees of freedom. When applied to plane Couette flow, it also captures

Reynolds stresses, the SSP and energy balance. Finally, it is important to highlight that DManD is highly advantageous because, like the underlying turbulent systems, it is a Markovian nature (where predictions of the next state only depend on the current state) and continuous-time formulation. Other non-Markovian frameworks with discrete-time formulation, such as recurrent neural networks and reservoir computing, have been shown to be effective in the modelling of chaotic dynamics (Pathak *et al.* 2018; Platt *et al.* 2022; Racca & Magri 2022).

The focus of this study is to build data-driven models in manifold coordinates for turbulent pipe flow. In the realm of turbulent pipe flow, most of the research on data-driven methods has focused on discerning coherent structures using POD (Hellström & Smits 2014; Hellström *et al.* 2016; Duggeby *et al.* 2007). POD effectively identifies the most energetic modes, and their corresponding streamwise and azimuthal wave numbers. Recently, Constante-Amores & Graham (2024) built reduced order models for an exact coherent state for pipe flow using POD first, followed by autoencoders to find the right embedding of the manifold. To date, however, there is an absence of data-driven low-dimensional models for effective time evolution of turbulent dynamics.

In this work, we address data-driven modeling for turbulent MFU pipe flow at $Re = 2500$. Pipe flow is characterised by a vast state space, thus, it requires dimension reduction to manifold coordinates. Then, we learn an evolution equation in this low-dimensional representation. We use these low-dimensional models to identify favorable initial conditions for the DNS in the search for new ECS. The rest of this paper is structured as follows. In section 2, we describe the framework for dimension reduction and time evolution. In section 3, we present the results that include the dimension reduction and the predictions of the DManD model for short- and long-time statistic, ECS identification, and new ECS found in the DNS using (nearly) converged ECS from the model as initial conditions. Finally, in Section 4, we summarize the concluding results.

2. Framework

2.1. Dimension reduction

While the state-space of a PDE is formally infinite-dimensional, the Navier-Stokes equations, which govern the motion of fluids, are dissipative in nature, and therefore solutions are expected to converge to a finite-dimensional invariant manifold, denoted as \mathcal{M} in this context (Temam 1989; Foias *et al.* 1988; Zelik 2022; Hopf 1948). This manifold \mathcal{M} exhibits a local Euclidean structure, implying that each point within it possesses a nearby region that can be bi-directionally mapped to and from a Euclidean space denoted as $\mathbb{R}^{d_{\mathcal{M}}}$, where $d_{\mathcal{M}}$ (with $d_{\mathcal{M}} \leq d_h$) represents the dimension of the manifold (e.g., in this work d_h is a higher dimension, in which the manifold can be embedded. This fact also what allows for the global coordinate representation, since dynamics are learned in d_h rather than $d_{\mathcal{M}}$). To effectively characterize this manifold and consequently understand the underlying system dynamics, only $d_{\mathcal{M}}$ independent coordinates are necessary, at least within local contexts. As \mathcal{M} remains unchanged by the system dynamics, the vector field on \mathcal{M} is always tangential to the manifold, leading to Markovian dynamics on \mathcal{M} . Then, these dynamics are governed by an ordinary differential equation defined by this tangential vector field.

We consider a system that is characterized by deterministic, Markovian dynamics, so if $\mathbf{u} \in \mathbb{R}^{d_N}$ represents the full space state, then the dynamics can be represented by an ODE as

$$\frac{d\mathbf{u}}{dt} = \mathbf{f}(\mathbf{u}). \quad (2.1)$$

here, \mathbf{u} represents the full state-space. In practice, u is obtained from a highly resolved direct numerical simulation (DNS). Then, we can find a mapping to a lower-dimensional representation

$$\mathbf{h} = \chi(\mathbf{u}), \quad (2.2)$$

where $\mathbf{h} \in \mathbb{R}^{d_h}$ is the low-dimensional representation of the full-state space, along with an approximation of its inverse

$$\tilde{\mathbf{u}} = \tilde{\chi}(\mathbf{h}), \quad (2.3)$$

so that the full state space may be recovered (e.g., ideally $\mathbf{u} \approx \tilde{\mathbf{u}}$). In this work, we opt to parameterise χ , $\tilde{\chi}$ with an undercomplete autoencoder, referred to as a hybrid autoencoder in Linot & Graham (2020). This hybrid autoencoder is based on the idea of using neural networks to learn the corrections from the leading POD coefficients

$$\mathbf{h} = \chi(\mathbf{u}; \theta_\varepsilon) = \mathbf{U}_{d_h}^T \mathbf{u} + \mathcal{E}(\mathbf{U}_r^T \mathbf{u}, \theta_\varepsilon), \quad (2.4)$$

here, $\mathbf{U}_k \in \mathbb{R}^{d_N \times k}$ corresponds to a matrix whose first k POD modes are ordered by variance, and \mathcal{E} corresponds to the encoder in the neural network. In this way, the first and second terms of the RHS stand for the projection onto the leading d_h POD modes, and the corrections provided by the neural network. The mapping back to the full space is given by

$$\tilde{\mathbf{u}} = \tilde{\chi}(\mathbf{h}; \theta_\varepsilon) = \mathbf{U}_r([\mathbf{h}, 0]^T + \mathcal{D}(\mathbf{h}; \theta_D)). \quad (2.5)$$

The weight parameters θ_E, θ_D are trained to minimize the loss

$$L = \frac{1}{dN} \sum_{i=1}^N \|\mathbf{u}(t_i) - \tilde{\chi}(\chi(\mathbf{u}(t_i); \theta_\varepsilon); \theta_D)\|^2 + \frac{1}{d_h N} \sum_{i=1}^N \kappa \|\mathcal{E}(\mathbf{U}_r^T \mathbf{u}(t_i); \theta_\varepsilon) + \mathcal{D}_{d_h}(\mathbf{h}(t_i); \theta_D)\|^2 \quad (2.6)$$

here, the first term corresponds to the mean-squared error of the reconstruction $\tilde{\mathbf{u}}$, while the second term corresponds to a penalty term to enhance the accurate representation of the leading d_h POD coefficients. In section 3.2, we also make use of standard autoencoders, which can be seen as $\mathbf{h} = \chi(\mathbf{u}; \theta_\varepsilon) = \mathcal{E}(\mathbf{U}_r^T \mathbf{u}, \theta_\varepsilon)$ and $\tilde{\mathbf{u}} = \tilde{\chi}(\mathbf{h}; \theta_\varepsilon) = \mathbf{U}_r^T \mathcal{D}(\mathbf{h}; \theta_D)$, to highlight the effectiveness of using the hybrid autoencoders to find an accurate representation of the manifold coordinates. We note that this undercomplete autoencoder has been used successfully for the Kuramoto-Sivashinsky equation, chaotic Kolmogorov flow, and MFU plane Couette flow (Linot & Graham 2020, 2023; Pérez-De-Jesús & Graham 2023).

To train both the hybrid and standard autoencoders, we use the Adam optimizer to minimize the loss function presented in Equation 2.6, utilizing the POD coefficients as inputs (as explained in section 3.2.1). The training process spans 500 epochs, and we incorporate a learning rate scheduler that reduces the learning rate from 10^{-3} to 10^{-4} after the initial 300 epochs. This adjustment is made based on our observation that no significant improvements in reconstruction error occur beyond this number of epochs. For the hybrid autoencoder approach, we set the hyperparameter $\kappa = 0.1$, while for the standard autoencoder, $\kappa = 0$ (indicating that this term is not included). Further details regarding the neural network architectures can be found in Table 1. The specific network parameters were determined through a meticulous try-and-error search, exploring variations in the network's architecture and activation functions. We remark, that our goal was to achieve the lowest reconstruction error while avoiding excessive computational costs. As pointed out by Linot & Graham (2023), the use of CNN does not hold any advantage with respect to dense neural networks on the POD basis (the

first stage for dimension reduction is to find the leading POD coefficients), as there are no longer spatial connections between the POD coefficients.

2.2. Time evolution: neural ODEs

We use a stabilized neural ODE framework for state space modeling in the latent space. Rather than equation 2.1, we use a slight modification:

$$\frac{d\mathbf{h}}{dt} = \mathbf{g}(\mathbf{h}) - \mathbf{A}\mathbf{h}. \quad (2.7)$$

here $\mathbf{A} = -\gamma\delta_{ij}\sigma_i(\mathbf{h})$, where $\sigma_i(\mathbf{h})$ stands for the standard deviation of the i th component of \mathbf{h} , γ is a fixed parameter and δ_{ij} is the Kronecker delta. This modification, with a small value of γ it has been found to stabilize the dynamics against spurious growth of fluctuations without compromising accuracy of predictions (Linot & Graham 2023; Linot *et al.* 2023a). The rationale behind introducing linear damping lies in the behavior of dissipative systems, where viscosity dampens the high wave numbers. In such systems, data located on the attractor exhibit a minimal content in these high wave numbers, and the incorporation of linear dampening becomes crucial as it enhances the stability of the trajectories and also aligns with the observed dynamics.

We integrate equation 2.7 forward in time from t_i to $t_i + \tau$ resulting in the prediction

$$\tilde{\mathbf{h}}(t_i + \tau) = \mathbf{h}(t_i) + \int_{t_i}^{t_i + \tau} \mathbf{g}(\mathbf{h}(t); \theta_g) - \mathbf{A}\mathbf{h}(t) dt, \quad (2.8)$$

We determine the parameters θ_g by minimising the difference between the true state $\mathbf{h}(t_i + \tau)$ and the the predicted state $\tilde{\mathbf{h}}(t_i + \tau)$, as

$$J = \frac{1}{d_h N} \sum_{i=1}^N \|\mathbf{h}(t_i + \tau) - \tilde{\mathbf{h}}(t_i + \tau)\|^2. \quad (2.9)$$

To calculate the derivatives of \mathbf{g} with respect to the parameters, we make use of automatic differentiation. We train the stabilised NODE to predict one-time unit of the centered data by using an Adam optimiser in PyTorch to minimise the loss function described in equation 2.9 (Paszke 2019). The training process incorporates a learning rate scheduler, which decreases at three evenly spaced intervals, continuing until the learning curve stabilizes. The specific details of this neural network are provided in Table 1. The architectural choices are empirical, determined through trial and error by varying the number of nodes and layers.

Once \mathbf{g} is determined, an arbitrary initial condition can be mapped into the low-dimensional coordinates with $\boldsymbol{\chi}$. Then, the state evolution of \mathbf{h} at arbitrary points in time can be computed as the solution to equation 2.7, and finally the solution can be mapped back to the full space with $\tilde{\boldsymbol{\chi}}$.

3. Results

In this section, we provide a detailed description of the dataset for MFU pipe flow, present the results of dimensionality reduction, evaluate the performance of the reduced models as we vary their dimension, and introduce new ECS. Figure 1a shows a three-dimensional representation of the MFU pipe configuration used in the current research. For visualisation purposes, the entire pipe is shown, although calculations in this work

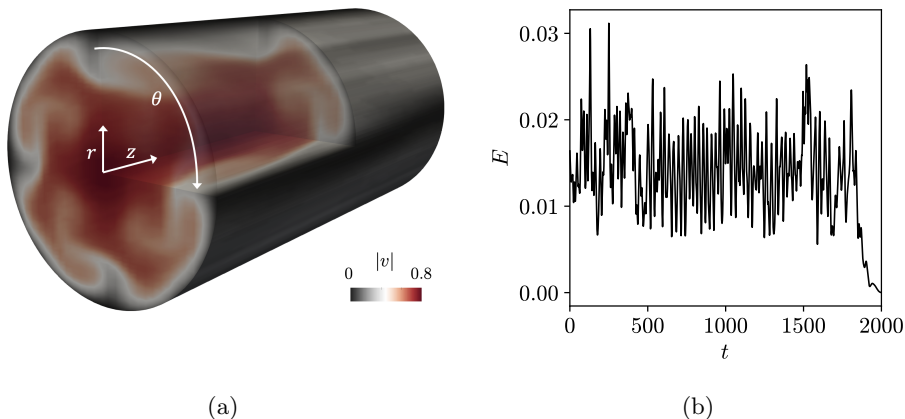


Figure 1: Schematic representation of the three-dimensional pipe flow system. Panel (a) shows a snapshot of the magnitude of the velocity field. For visualisation purposes, the entire pipe is shown, although calculation in this work is restricted in the shift-and-reflect symmetry subspace with $m_p = 4$ (which is the highlighted area with opacity). Panel (b) represents the energy in the axially dependent modes only (k non-zero). This quantity decays rapidly after relaminarisation.

are confined to the shift-and-reflect symmetry subspace (which is the highlighted area with opacity).

3.1. Description of pipe flow data

We perform DNS of an incompressible viscous fluid moving inside of a pipe with a circular cross-section. We consider flow with a constant max flux, thus, the dimensionless forms of the Navier-Stokes equations are expressed as

$$\frac{\partial \mathbf{v}}{\partial t} + \mathbf{U} \cdot \nabla \mathbf{v} + \mathbf{v} \cdot \nabla \mathbf{U} + \mathbf{v} \cdot \nabla \mathbf{v} = -\nabla p + 32 \frac{\beta}{Re} \mathbf{z} + \frac{1}{Re} \nabla^2 \mathbf{v},$$

$$\nabla \cdot \mathbf{v} = 0. \quad (3.1)$$

The equations are solved in cylindrical coordinates (r, θ, z) which refer to the radial, azimuthal and the streamwise (axial) directions, respectively. Here, \mathbf{v} and p stand for the velocity and the pressure, respectively. The Reynolds number Re is defined as $Re = U\mathcal{D}/\nu$, where U , \mathcal{D} and ν are the mean flow velocity, the pipe diameter and the kinematic viscosity, respectively. Lengths and velocities are made non-dimensional using \mathcal{D} and U as characteristic values, and hence, time will be made non-dimensional using \mathcal{D}/U . The velocity $\mathbf{v} = (v_r, v_\theta, v_z)$ represents the deviation from laminar Hagen-Poiseuille flow equilibrium $\mathbf{U}(r) = 2(1 - (2r)^2)\mathbf{z}$. To maintain constant mass flux, a pressure gradient is required, and the excess pressure needed is measured by the feedback variable $\beta = \beta(\mathbf{v})$; thus the total dimensionless pressure gradient is $(1 + \beta)(32/Re)$, and $\beta = 0$ for laminar flow.

In the NSE, symmetries appear in the form of continuous and discrete symmetry groups. For the former, the cylindrical wall in pipe flow limits rotational symmetry around the z -axis and restricts translational movement along it. Let $\sigma_z(\phi, \ell)$ represent the shift operator, where $\sigma_z(\phi, 0)$ signifies an azimuthal rotation by ϕ around the pipe axis, and $\sigma_z(0, \ell)$ indicates streamwise translation by ℓ . Let σ_θ represent the reflection about the

$\theta = 0$ azimuthal angle:

$$\left. \begin{aligned} \sigma_z(\phi, \ell)[v_r, v_\theta, v_z, p](r, \theta, z) &= [v_r, v_\theta, v_z, p](r, \theta - \phi, z - \ell) \\ \sigma_\theta[v_r, v_\theta, v_z, p](r, \theta, z) &= [v_r, -v_\theta, v_z, p](r, -\theta, z) \end{aligned} \right\}$$

Apart from azimuthal reflection, NSE also have additional discrete symmetries in both azimuthal and streamwise directions across the computational cell Ω . The symmetry group of streamwise periodic pipe flow is $SO(2)_z \times O(2)_\theta$. In this paper, we restrict the dynamics to the 'shift-and-reflect' symmetry subspace

$$S = \{e, \sigma_\theta \sigma_{z_s}\}, \quad (3.2)$$

where σ_{z_s} represents a streamwise shift by $L/2$, i.e., flow fields of equation 3.1 that satisfy

$$[v_r, v_\theta, v_z, p](r, \theta, z) = [v_r, -v_\theta, v_z, p](r, -\theta, z - L/2). \quad (3.3)$$

This symmetry couples the streamwise translations with the azimuthal reflection. By imposing the shift-reflect symmetry, eliminates the continuous phase along the azimuthal rotations. In this work, we do not factor out the continuous symmetry in the streamwise direction.

To perform the DNS of the incompressible turbulent pipe flow under the assumption of shift-and-reflect symmetry, we use the pseudo-spectral code Openpipeflow (Willis 2017). Fourier discretization is used for the periodic axial (z) and azimuthal (θ) directions, with K and M representing the number of Fourier modes, i.e.,

$$\{\mathbf{v}\}(r, \theta, z, t) = \sum_{m=-M}^M \sum_{k=0}^K \mathbf{B}_{mk}(r, t) e^{im_p m \theta} e^{ik\alpha z}, \quad (3.4)$$

here $\mathbf{B}_{mk}(r, t)$ represents a three-vector of Fourier amplitudes, m_p is a parameter to account for shift-invariant in the azimuthal direction, and $\alpha = 2\pi/L$ is a parameter that controls the length of the pipe. In the radial direction, a Chebyshev grid is used that cluster points near the wall to effectively resolve the velocity gradients. No-slip and no-penetration boundary conditions are enforced at the wall (i.e., $r/R = 1$). For a more detailed description of the numerical method, we refer to Willis (2017).

The simulation of the entire cross-sectional pipe ($m_p = 1$) presents a naturally periodic azimuthal boundary condition, while other values of m_p result in \mathbf{v} repeating itself in the azimuthal direction. In this work, we construct models for MFU pipe flow at $Re = 2500$, with $m_p = 4$ ('shift-and-reflect' invariant subspace) and $\alpha = 1.7$, as previous work done by Willis *et al.* (2013) and Budanur *et al.* (2017). Then, the size of the computational cell is described by

$$\Omega^+ = [1/2, 2\pi/m_p, \pi/\alpha] \equiv (r, \theta, z) \in [0, 1/2] \times [0, 2\pi/m_p] \times [0, \pi/\alpha]. \quad (3.5)$$

Thus, the domain size in wall units for the wall-normal, azimuthal, and streamwise dimensions is $\Omega^+ \approx [100, 160, 370]$, respectively, which compares well with the minimal flow units for Couette flow and plane Poiseuille flow (i.e., $\Omega^+ \sim [68, 128, 190]$ and $\Omega^+ \approx [> 40, 100, 250 - 300]$, respectively). This domain size is similar to that used in the minimal box simulation by Jiménez & Moin (1991) and Willis *et al.* (2013), and it is sufficiently large to exhibit complex chaotic behavior.

Data were generated with $\delta t = 0.01$ on a grid $(N_r, M, K) = (64, 10, 14)$. Following the 3/2 rule, variables are evaluated on $64 \times 30 \times 42$ grid points; thus, $\mathbf{u} \in \mathbb{R}^{241,920}$. In this grid size, $(\Delta\theta D/2)^+ \approx 5.3$ and $\Delta z^+ \approx 8.8$ (which is consistent with grid sizes used by Jiménez & Moin (1991)). The resolution was tested to ensure mesh-independent results, confirmed by a drop in the energy spectra by at least 4 orders of magnitude.

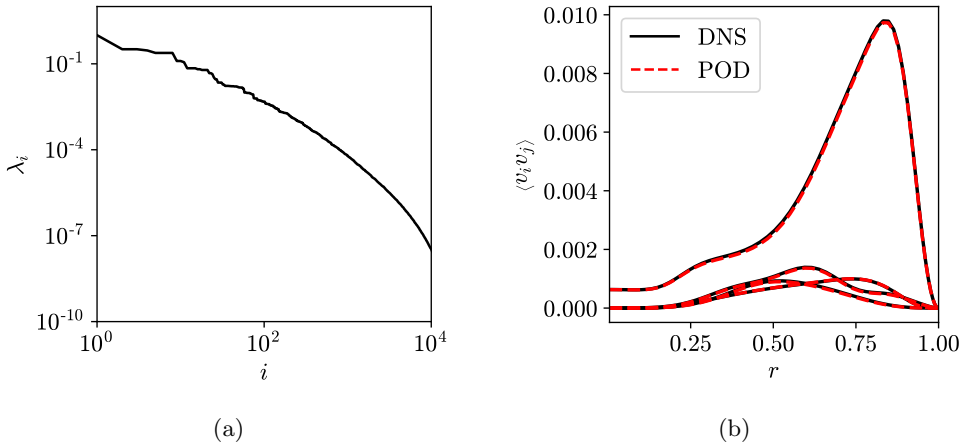


Figure 2: (a) Eigenvalues of the POD modes sorted in descending order. (b) Reconstruction of four components of the Reynolds stresses from the DNS and the data projected onto 512 POD modes. The curves correspond to $\langle u_z^2 \rangle$, $\langle u_\theta^2 \rangle$, $\langle u_r u_z \rangle$ and $\langle u_\theta^2 \rangle$, from top to bottom, respectively.

We initiated simulations from random divergence-free initial conditions. The first initial condition comes from a short-period RPO with a period $T = 26.649$ for MFU pipe flow at $Re = 2500$, $m_p = 4$, $\alpha = 1.7$, which is part of the database of Openpipeflow (Willis 2017). The solutions were evolved forward in time for either 10,000 time units or until relaminarization occurred. The initial 100 time units were excluded as transient data, and the final 200 time units were excluded if relaminarization had occurred. Figure 1b plots the energy in the axially dependent modes only (k non-zero), which decays rapidly after relaminarization, indicating the end of the simulation. This process was repeated with new initial conditions until we accumulated 96,921 time units of data, sampled at one-time unit intervals (*i.e.*, $\tau = 1$). Consequently, all data live in the turbulent attractor. We divided this dataset, allocating 80% for training and 20% for testing purposes.

3.2. Learning of manifold coordinates

In this section, we present our approach to dimensionality reduction. We first apply linear reduction using POD, and then proceed with nonlinear reduction using autoencoders.

3.2.1. Linear dimension reduction with POD: From $\mathcal{O}(10^5)$ to $\mathcal{O}(10^3)$

The first step in constructing the low-dimensional model is the use of POD on the original dataset as a preprocessing step. This aims to reduce the dimension of the problem from approximately $\mathcal{O}(10^5)$ degrees of freedom to $\mathcal{O}(10^3)$, while preserving the essential characteristics of the turbulent flow system. POD tries to find the function Φ that maximizes

$$\frac{\langle |\mathbf{v}', \Phi|^2 \rangle}{\|\Phi\|_E^2}, \quad (3.6)$$

where $\langle \cdot \rangle$ is the ensemble average, and the inner product is defined to be

$$(\mathbf{q}_1, \mathbf{q}_2)_E = \int \int \int \mathbf{q}_1 \cdot \mathbf{q}_2 d\mathbf{x} \quad (3.7)$$

with the corresponding energy norm $\|\mathbf{q}\|_E = (\mathbf{q}_1, \mathbf{q}_2)_E$. Solutions $\Phi^{(n)}$ to this problem satisfy the eigenvalue problem

$$\int_0^L \int_0^{2\pi/m_p} \int_0^R \langle \mathbf{v}'(\mathbf{x}, t), \mathbf{v}^*(\mathbf{x}', t) \rangle r' dr' d\theta' dz' = \lambda \Phi^{(n)}, \quad (3.8)$$

where $\mathbf{v}(\mathbf{x}) = \mathbf{v}'(\mathbf{x}) - \bar{\mathbf{v}}(\mathbf{x})$ stands for the fluctuating component of the velocity field, and $\bar{\mathbf{v}}$ is the mean velocity, obtained by averaging over both space and time.

The eigenvalue problem described by equation 3.8 becomes $n \times n$ (where $n = 3 \times N_r \times 3M \times 3K = 241,920$). To reduce the computational cost of this eigenvalue problem, and preserve symmetries, we treat the POD modes as Fourier modes in both the azimuthal and streamwise directions. This approach has been previously applied by Duggleby *et al.* (2007) and Linot & Graham (2023) for turbulent pipe and plane Couette flow, respectively. Thus, the eigenvalue problem becomes

$$\int_0^R \langle \hat{\mathbf{v}}(k_\theta, k_z; r), \hat{\mathbf{v}}(k_\theta, k_z; r') \rangle \varphi^{*(n)}(k_\theta, k_z; r') r' dr' = \lambda_{k_\theta k_z}^{(n)} \varphi^{(n)}(k_\theta, k_z; r), \quad (3.9)$$

where $*$ denotes the complex conjugate, λ is the eigenvalue, and $\hat{\mathbf{v}}(k_\theta, k_z; r)$ is the Fourier transform of the fluctuating velocity in the azimuthal and axial direction. Thus, the eigenvalue problem is reduced from $n \times n$ to a $3N_r \times 3N_r$ problem for each pair of wavenumbers (k_θ, k_z) in the Fourier coefficients. This analysis gives us POD modes represented by

$$\Phi_{k_\theta k_z}^{(n)}(r, \theta, z) = \varphi^{(n)}(k_\theta, k_z; r) e^{ik_\theta \theta} e^{i2\pi k_z z/L}. \quad (3.10)$$

The projection onto these modes results in complex values unless both k_θ and k_z are zero. We arrange the modes in descending order of their eigenvalues (λ_i), and we select the leading 512 modes, resulting in a vector of POD coefficients ($\mathbf{a}(t)$). Most of these modes are characterised by being complex (i.e., they have 2 degrees of freedom), so projecting onto these modes results in a 1014-dimensional system, i.e., $d_{POD} = 1014$. In figure 2a, we display the eigenvalues revealing a rapid decline followed by a long tail that contributes minimally to the energy content. By dividing the sum of the eigenvalues of the leading 512 modes by the total sum, we find these modes account for 99.83% of the energy. Illustratively, figure 2b displays the reconstruction of Reynolds stresses for the components $\langle v_z^2 \rangle$, $\langle v_\theta^2 \rangle$, $\langle v_r v_z \rangle$ and $\langle v_r^2 \rangle$, from top to bottom, respectively. This reconstruction is obtained by using those 512 modes with 5000 snapshots. We observe an excellent agreement between the DNS and the flow field obtained after truncating to the leading POD modes.

3.2.2. Nonlinear dimension reduction with autoencoders: From $\mathcal{O}(10^3)$ to $\mathcal{O}(10^1)$

After converting the data to the leading POD modes, and selectively retaining only the high-energy coefficients, our next step involves a nonlinear reduction of the data using autoencoders. As a crucial preprocessing step, we normalize the POD coefficients by subtracting the mean and dividing by the maximum standard deviation, rather than dividing by the standard deviation of each component. The rationale behind this choice is that the standard deviation of high-order POD coefficients tends to contribute less to the overall reconstruction compared to the low-order POD coefficients.

Figure 3a shows the relative error on the test data of the POD coefficients using standard and hybrid autoencoders when varying $10 < d_h < 20$. We have also added the corresponding values from a linear projection onto an equivalent number of POD

Function	Shape	Activation	Learning Rate
χ	1014/2500/1000/500/100/ d_h	ReLU/ReLU/ReLU/ReLU/lin	$[10^{-3}, 10^{-4}]$
$\tilde{\chi}$	$d_h/100/500/1000/2500/1014$	ReLU/ReLU/ReLU/ReLU/lin	$[10^{-3}, 10^{-4}]$
\mathbf{g}_{NN}	$d_h/250/250/250/250/d_h$	sig/sig/sig/sig/lin	$[10^{-2}, 10^{-3}]$

Table 1: Neural network architectures for the autoencoder and NODE. ‘Shape’ represents the dimension of each layer, ‘Activation’ refers to the types of activation functions used, where ‘ReLU’, ‘sig’ and ‘lin’ stand for ReLU, sigmoid and linear activation functions, respectively. ‘Learning Rate’ represents the learning rate at various times during training.

coefficients. The POD projection onto the leading (complex) coefficients can be expressed as $\mathbf{a} = \mathbf{U}_r^T \mathbf{u}$. For each dimension, two autoencoders are trained to reduce the stochastic behavior of the optimisation. The same architectures are used for the standard and hybrid autoencoders (see table 1).

In Figure 3a, the nonlinear reduction leads to nearly one-order-of-magnitude decrease in the value of mean squared error (MSE) compared to its equivalent with PCA for the same dimensionality. Notably, a discernible reduction in error is observed beyond a threshold of $d_h > 17$. Beyond this point, the relative error appears to plateau with a minimum MSE reduction), suggesting that the autoencoders are capable of finding a mapping from the full space to a low-dimensional representation. This implies that, with dimensions as few as 17, the autoencoders could provide with good coordinate transformation from the full space. In all considered cases, the hybrid autoencoder consistently produces slightly better results in terms of MSE compared to the standard autoencoders. In Figure 3b, we compare the performance of both autoencoders by plotting the mean-squared POD coefficient amplitudes for the test data, denoted as $\langle \|a_n\|^2 \rangle$, for the low-dimensional representation with $d_h = 20$ (see figure 3b). The hybrid autoencoder exhibits limitations in capturing the amplitude of higher-order coefficients beyond $\mathbf{a} > 30$, while the standard autoencoder struggles to accurately represent coefficients beyond the first two. This discrepancy arises from the fact that the undercomplete autoencoder prioritizes the reconstruction of the leading d_h POD coefficients. Figure 3c illustrates the Reynolds stresses for both types of autoencoders with $d_h = 20$ for 5000 snapshots of the test data, showing that the hybrid autoencoder outperforms the standard autoencoder. Finally, figure 3d displays field snapshots in the $z - \theta$ plane ($r = 0.496$) at random times showing qualitatively that hybrid autoencoders with $d_h = 20$ can accurately reconstruct the data.

Lastly, it is important to note that ideally the relative error value would plateau after determining the ‘right’ manifold dimension yet it is not always feasible, primarily due to computational limitations introduced during the training process. Our goal is to identify the optimal dimension for constructing DManD models that faithfully capture both short-time tracking and long-time statistical characteristics of turbulent pipe flow. In the upcoming section, we will systematically build models with varying latent dimension sizes.

3.3. Modelling in manifold coordinates

Following the training of the autoencoders, a comprehensive exploration of the dampening parameter γ is conducted to prevent the dynamics drifting away from the attractor

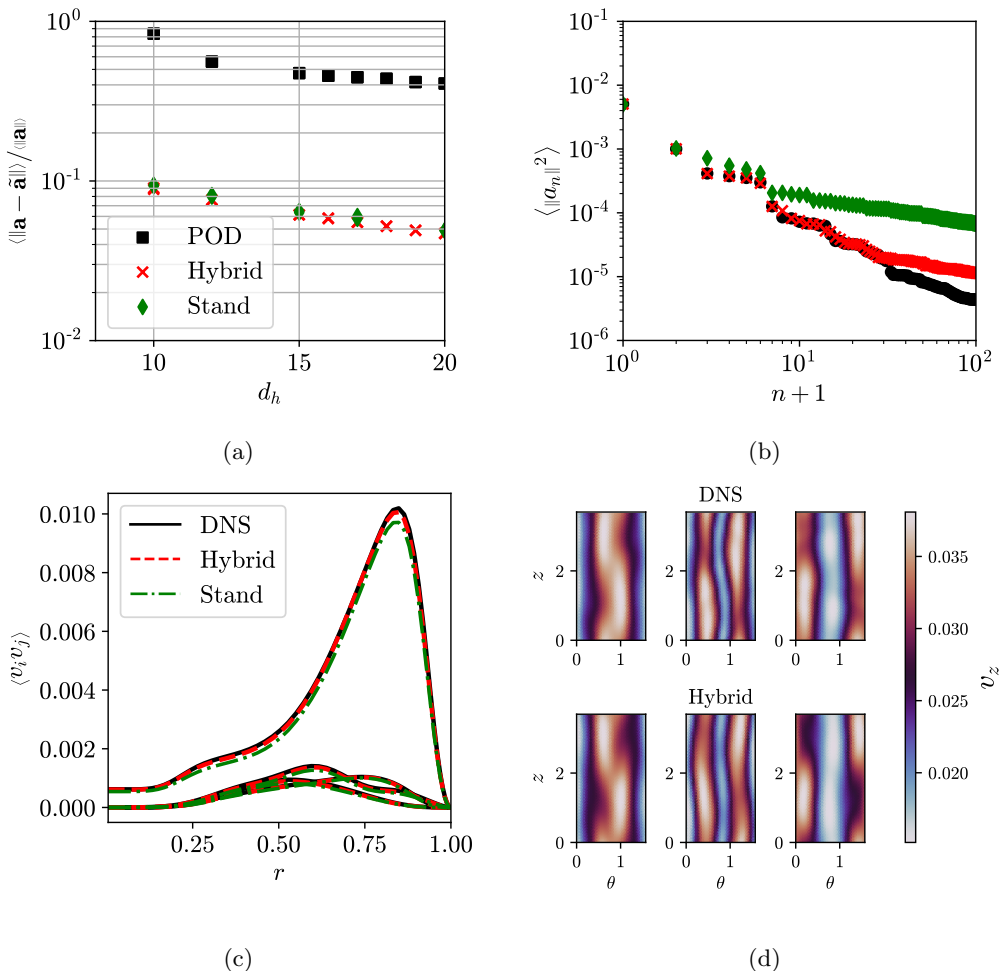


Figure 3: Nonlinear reduction with autoencoders: (a) Relative error on test data for POD coefficients, standard and hybrid autoencoders as a function of the latent dimension d_h . For each dimension, results for two standard and two hybrid autoencoders are reported. (b) Reconstruction of $\langle \|a_n\|^2 \rangle$ (mean-squared POD coefficient amplitudes) for the test data from 512 POD modes and the standard and hybrid autoencoders at $d_h = 20$. (c) Components of the Reynolds stresses from the DNS and using autoencoders with $d_h = 20$. (d) Two-dimensional representation of the flow field in a $z-\theta$ plane ($r = 0.496$) with u_z for the DNS and reconstructed using the hybrid autoencoder at $d_h = 20$.

during modelling. To find the optimal value of γ , trials are performed with $d_h = 20$, varying γ within the range $0.1 < \gamma < 0.5$. Empirical findings consistently point towards $\gamma = 0.25$ yields superior outcomes. We note that the significance of γ has been rigorously investigated by Linot & Graham (2023), in the context of MFU plane Couette flow. The training objective of the NODE is focused on predicting one time unit ahead ($\tau = 1$), as described by equation 2.8. As a preprocessing step for training the NODE, we subtract the mean of the latent space of the autoencoders as centralizing. This centralization ensures that the linear damping effectively guides trajectories towards the origin.

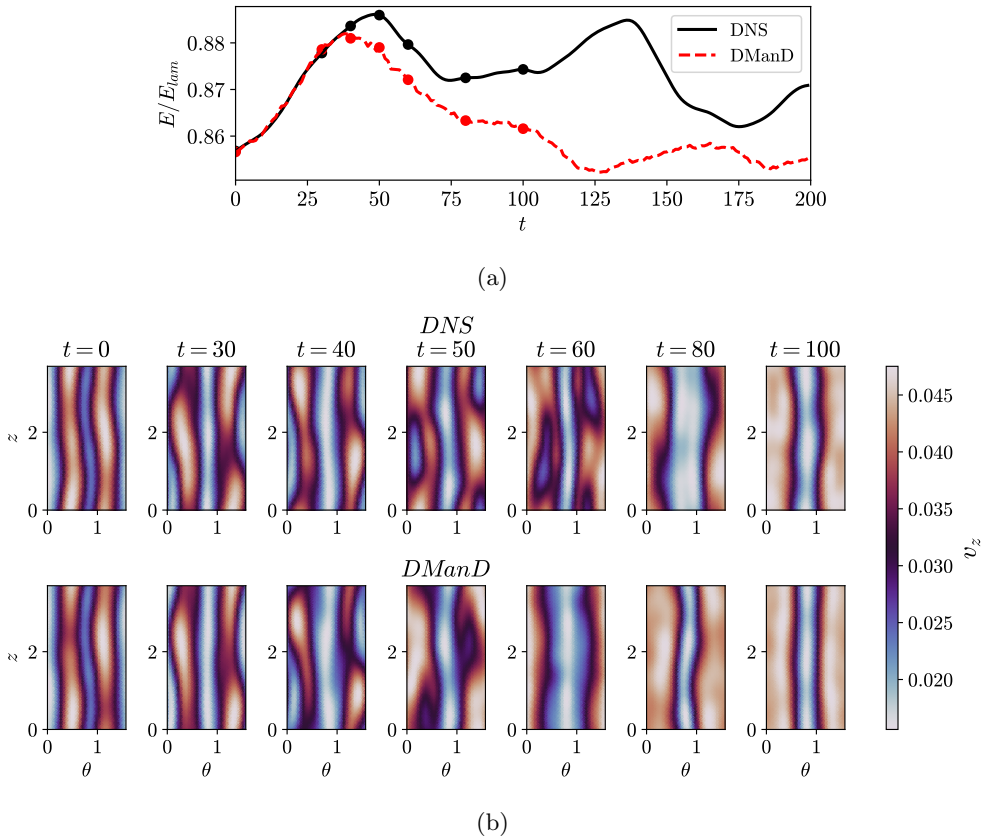


Figure 4: (a) Normalised kinetic energy of the system for the DNS and DManD model with $d_h = 20$ up to $t = 200$. (b) Two-dimensional representation of the dynamics in the $z - \theta$ plane ($r = 0.496$) with u_z for the DNS and DManD model. Time is displayed at the top of each panel, corresponding to the marked dots in panel (a). We refer the reader to the supplemental materials to view a video of this trajectory.

Unless otherwise specified, the results presented showcase the top-performing model at each dimension, with the lowest relative error averaged across all considered statistics. It is crucial to note that, for all DNS versus DManD model comparisons at each d_h , identical initial conditions are applied in the models. From the perspective of the DManD models, this involves encoding the initial condition from the DNS, and subsequently evolving it forward on time in the latent space to generate a time series of \mathbf{h} . This time series is then decoded to the full state space for comparative analysis.

3.3.1. Short-time tracking

In this section, we evaluate the performance of the DManD models in reconstructing short-time trajectories. Figure 4a shows the time evolution of the kinetic energy of the system for the DNS and DManD model with $d_h = 20$. Here, the kinetic energy of the

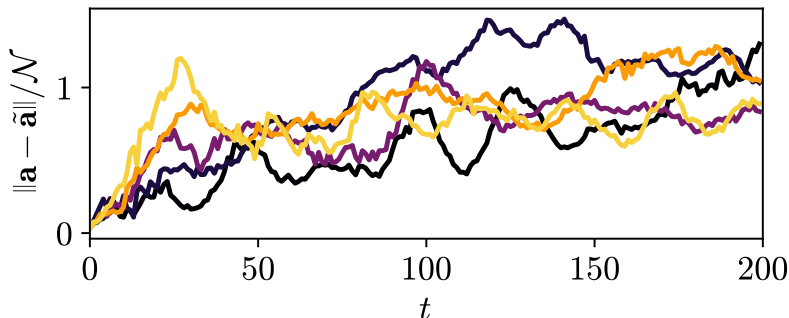


Figure 5: Normalised short-time-tracking error for five arbitrary initial conditions using DManD with $d_h = 20$ up to $t = 200$.

system is given by the L^2 inner product

$$E = \frac{1}{\mathcal{V}} \int_0^{2\pi/\alpha} \int_0^{2\pi/m_p} \int_0^r \frac{1}{2} \mathbf{v} \cdot \mathbf{v} r \, dr d\theta dz \quad (3.11)$$

where \mathcal{V} corresponds to the cylindrical flow domain. The results displayed in figure 4a are normalized by the kinetic energy of the laminar state. We have selected $d_h = 20$ as it represents the minimum dimension that yields superior results for both short-term and long-time measures, as will be demonstrated in this and the subsequent sections. We note that $d_h = 20$ may not necessarily correspond to the right dimension of the manifold, but this corresponds to the smallest dimension that can faithfully capture the nonlinear dynamics of the turbulent pipe flow. We reiterate that we have commenced from an initial state dimension of $\mathcal{O}(10^5)$. Figure 4a shows that DManD model can generate predictions which capture the true dynamics of the system up to $t \sim 50$. To provide a more qualitative representation of the model dynamics, figure 4b displays a two-dimensional representation of the dynamics in the $z - \theta$ plane ($r = 0.496$) with v_z for the DNS and DManD model. We observe a good agreement between the model and the DNS. We refer the reader to the supplementary materials to view a video from this trajectory.

The initial condition for figure 4 is selected because it qualitatively represents the Self-Sustaining Process (SSP) where streamwise rolls, streaks, and wavelike disturbances mutually sustain each other, counteracting viscous decay. In the true system (top panels of figure 4b), streaks (velocity functions below the mean) near the wall at the center of the domain (see $t = 0$) are affected by azimuthal wavy disturbances, leading to their breakdown and the formation of rolls (see $t = 30 - 60$). These rolls, in turn, induce the re-emergence of streaks (see $t = 80$). DManD qualitatively captures these dynamics (see the corresponding bottom panels) with a slightly accelerated breakdown of the rolls into streaks.

While figure 4 only shows the trajectory for one selected initial condition, figure 5 represents the tracking error for five random initial trajectories at $d_h = 20$. Here we plot $\|\mathbf{a}(t) - \tilde{\mathbf{a}}(t)\|_2^2 / \mathcal{N}$, where \mathcal{N} denotes the error of true solutions at random times t_i and t_j , i.e., $\mathcal{N} = \langle \|\mathbf{a}(t_i) - \mathbf{a}(t_j)\| \rangle$. To enhance computational efficiency, we opted for comparisons in POD coefficients rather than velocity fields. This decision was motivated by the computationally intensive nature (i.e., memory usage) of reconstructing fields

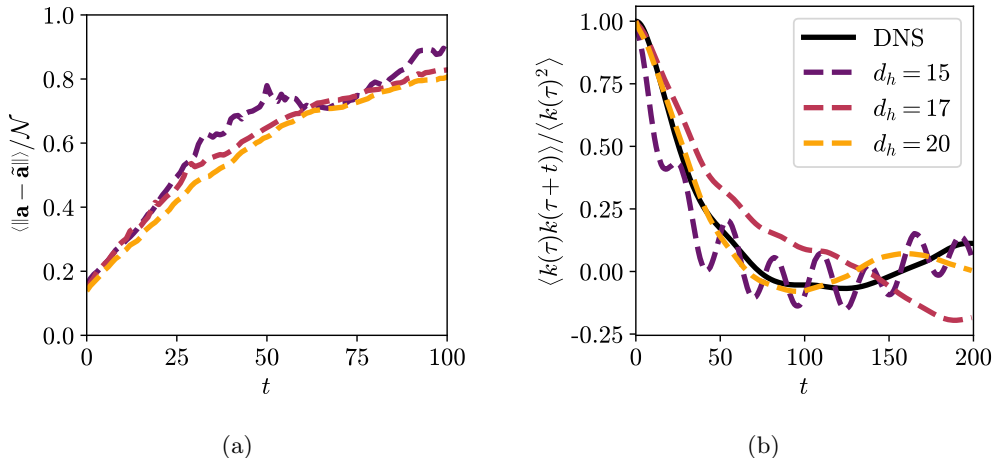


Figure 6: Short-time tracking performance: (a) Ensemble-averaged of 500 random initial conditions as a function of d_h . (b) Temporal autocorrelation of fluctuations in the kinetic energy as a function of d_h . The black solid line represents the temporal autocorrelation calculated in the DNS. For representation purposes, we only show results for $d_h = [15, 17, 20]$.

from POD coefficients. Moreover, the POD coefficients enable the capture of the 99.83% of the energy within the system (with 512 POD modes). Figure 5 shows that for certain initial conditions, the error remains relatively low until $t = 50$, after which it increases before stabilizing at unity at longer times, in line with expectations.

Next, we conduct a parametric study on the normalized ensemble-averaged tracking error for DManD models by varying the dimension of the latent space (see figure 6a). We used 500 random initial conditions evolved over 100 time units. Notably, we observe that when the dimensionality surpasses 17 ($d_h > 17$), the tracking errors converge, indicating that a dimension of at least 17 is required for a better field reconstruction.

To understand the short-time tracking and the correlation of the models with different initial conditions, we will plot the autocorrelation of fluctuations of the kinetic energy. We define its fluctuating part as $k(t) = E(t) - \langle E \rangle$. In figure 6, we plot the temporal autocorrelation of k with respect to its corresponding initial condition for 6000 random initial conditions evolved up to $t = 200$. It is not until $d_h = 20$, that the predicted autocorrelation matches reasonably well up to $t \sim 120$ with respect to the true data.

3.3.2. Long-time statistics

This section is dedicated to presenting the long-time statistics predictions for the DManD models. To evaluate the long-time performance of the DManD models, we first use the $\langle |a_n|^2 \rangle$ metric, plotting it for a long trajectory (up to 3000-time units) in both the DNS solution and the predicted trajectories from DManD at $d_h = 20$ (see figure 7). We observe that DManD demonstrates a good match with the true solution up to the first 30 leading POD coefficients of the true solution. This observation implies a robust capability of DManD to capture the intricate nonlinear dynamics of the system over an extended time span. To establish a meaningful comparison of this framework, we draw parallels with classical methods for reduced order models proposed by Gibson (2002) for Couette flow (i.e., POD-Galerkin). Gibson (2002) required between 512 (~ 1000 degrees

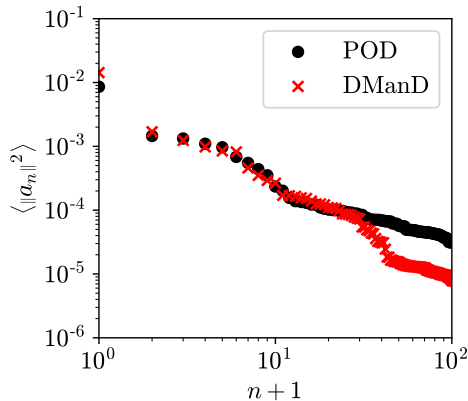


Figure 7: Comparison of $\langle \|a_n\|^2 \rangle$ for the DNS and DManD at $d_h = 20$ for the same initial condition evolved 3000 time units.

of freedom) and 1024 modes (~ 2000 degrees of freedom) to achieve a reliable prediction of the leading 30 POD coefficients for plane Couette flow.

We turn our attention to the predictions of various models concerning the Reynolds stresses, as illustrated in figure 8. The streamwise velocity component $\langle u_z^2 \rangle$ is the most important component with a peak near the wall, being one order of magnitude bigger than the other components. We observe that our DManD models demonstrate strong performance in predicting the Reynolds stresses of the system beyond $d_h > 17$. At $d_h = 20$, in particular, DManD exhibits exceptional performance by closely matching three out of the four displayed components. However, some small discrepancies are observed in the component corresponding to $\langle u_\theta^2 \rangle$.

Next, we assess how well the DManD models are capable of reconstructing the energy balance at long times by examining the joint probability density functions of power input (I) and dissipation (D). The power input required to maintain constant flux mass and dissipation due to viscosity are defined as

$$I = \frac{1}{\mathcal{A}} \int_0^{2\pi/\alpha} \int_0^{2\pi/m_p} \left| \frac{\partial v_z}{\partial r} \right|_{r=R} d\theta dz, \quad (3.12)$$

$$D = \frac{1}{\mathcal{V}} \int_0^{2\pi/\alpha} \int_0^{2\pi/m_p} \int_0^r |\nabla \times \mathbf{v}|^2 r dr d\theta dz. \quad (3.13)$$

here \mathcal{V} and \mathcal{A} stand for the volume and area of the pipe, respectively. In the results shown in this paper, the energy input and dissipation values are normalized by their laminar values. An energy balance can be derived from the inner product $\langle \mathbf{v}, \partial \mathbf{v} / \partial t \rangle$ (Waleffe 2001). Then, the energy input rate, the dissipation rate, and the kinetic energy $\bar{E} = (I - D)/Re$, which must average to zero over long times. It is imperative to ensure that this quantity averages to zero over extended periods, signifying equilibrium. This assessment is pivotal in affirming the accuracy of DManD models in maintaining energy balance.

Figure 9 display the joint PDFs of the normalised D and I from the DNS, and DManD

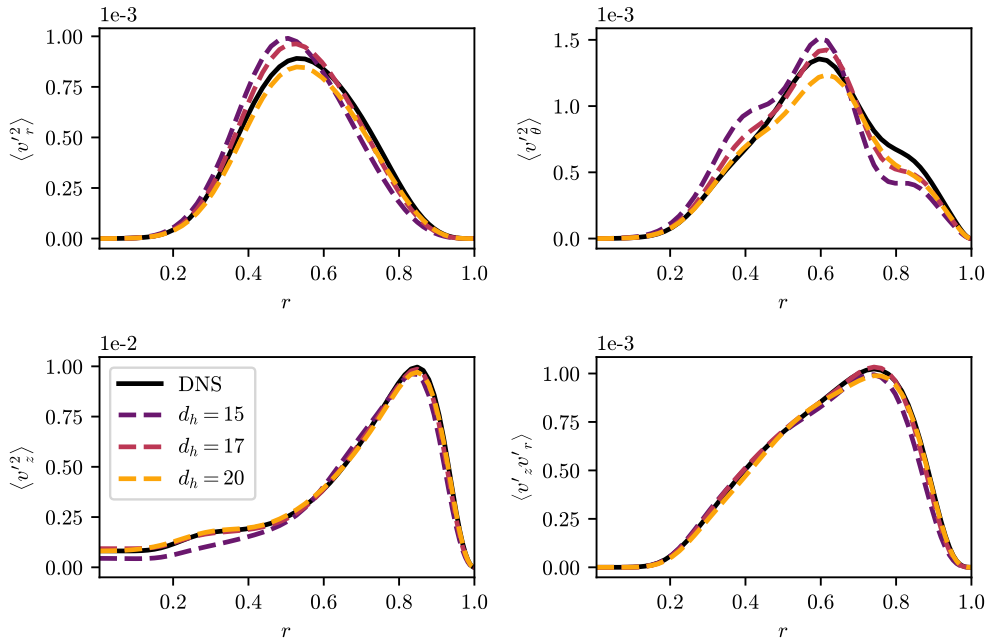


Figure 8: Long-time statistics: Components of the Reynolds stresses with increasing dimension for DManD models at various dimensions. The black solid lines represent the Reynolds stresses calculated in the DNS. For clarity, we only show results for $d_h = [15, 17, 20]$.

models with $d_h = 15$ and $d_h = 20$, generated from a long time trajectory evolved up to 3000 time units (with the same initial condition). For $d_h = 15$, the model fails to capture the intrinsic nonlinear dynamics of the system, but for $d_h = 20$, the model accurately captures the core region of these projections, including the excursions occurring at high dissipation rates that are also present in the DNS results. Overall, we can conclude that DManD can effectively predict accurately the long-time statistics of this complex system in the coordinates of the low-dimensional representation.

To further quantify the divergence between the PDFs from the DNS and DManD, we calculate the earth movers distance (EMD) as a function of the dimension of the low-dimensional model. The EDM measures the distance between two PDFs by framing the true PDF as the ‘supplies’ and the DManD model PDF as the ‘demands’. It seeks to minimize the effort required to transport the supplies to meet the demands, essentially solving a transportation problem. We find the flow f_{ij} that minimises $\sum_{i=1}^m \sum_{j=1}^n f_{ij} d_{ij}$ subject to the constrains

$$f_{ij} \geq 0, \quad 1 \leq i \leq m, \quad 1 \leq j \leq n, \quad (3.14)$$

$$\sum_{j=1}^n f_{ij} = p_i \quad 1 \leq i \leq m, \quad (3.15)$$

$$\sum_{i=1}^m f_{ij} = q_j \quad 1 \leq j \leq n. \quad (3.16)$$

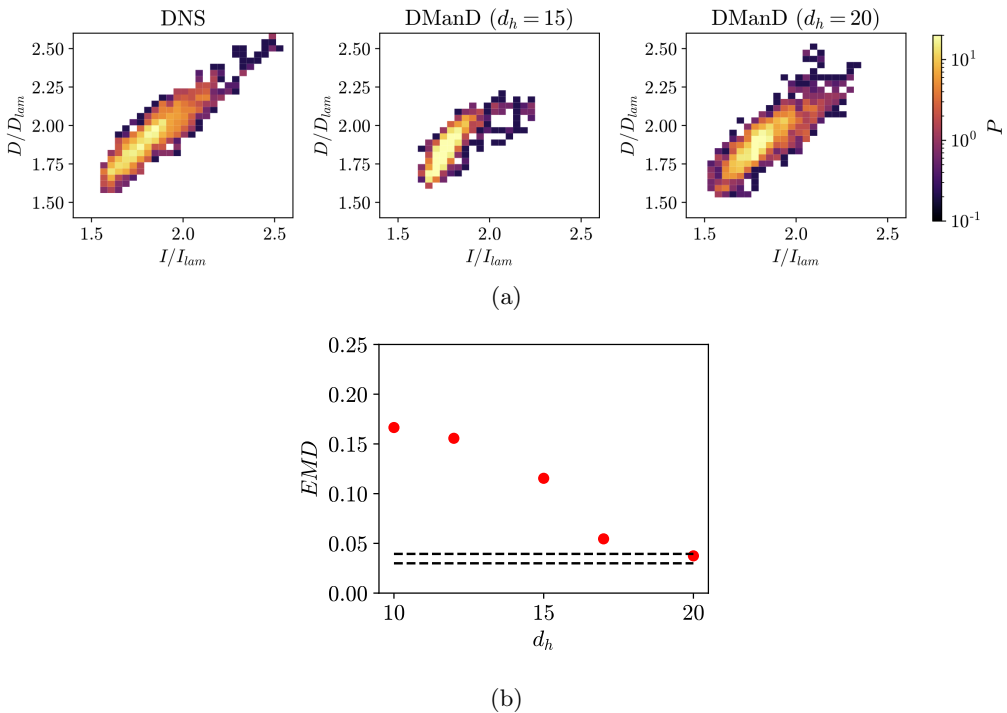


Figure 9: Energy balance: (a) Joint PDFs of the dissipation (D) and power input (I) for the true system, and the DManD models at $d_h = 15$ and $d_h = 20$, corresponding to columns one to three, respectively. (b) Earth movers distance (EMD) between the PDF from the DNS and the PDF predicted by the DManD model at various dimensions d_h . The dashed lines represent the error between two PDFs generated from DNS trajectories of the same length but with different initial conditions.

Here, p_i represents the probability density at the i th bin in the model PDF, and q_j is the probability density at the j th bin in the DNS PDF, where both PDFs are discretized into n and m bins (in this scenario, $n = m$). Additionally, d_{ij} denotes the cost associated with moving between bins, with the L_2 distance between bins i and j serving as the measure (where $d_{ij} = 0$ for $i = j$). After solving the minimization problem to determine the optimal flow f_{ij}^* , the EMD is calculated as

$$EMD = \frac{\sum_{i=1}^m \sum_{j=1}^n f_{ij}^* d_{ij}}{\sum_{i=1}^m \sum_{j=1}^n f_{ij}^*} \quad (3.17)$$

Figure 9b shows the EMD values depending on the latent dimensions, with all DManD models starting from the same initial condition and evolved up to 3000 time units. Additionally, we include the error when comparing two PDFs generated from the DNS with different conditions (dashed lines). Figure 9b demonstrates that the addition of latent dimensions results in an enhancement of the EDM value. Specifically, for $d_h = 20$, the DManD model reaches a level of comparability to the DNS. This observation, combined with short-time tracking, supports the assertion that only 20 degrees of freedom are necessary to create low-dimensional models that faithfully capture both the short-time tracking and long-time statistics of the nonlinear turbulent dynamics of MFU pipe flow at $Re = 2500$. It is important to note that we are not asserting a specific dimension

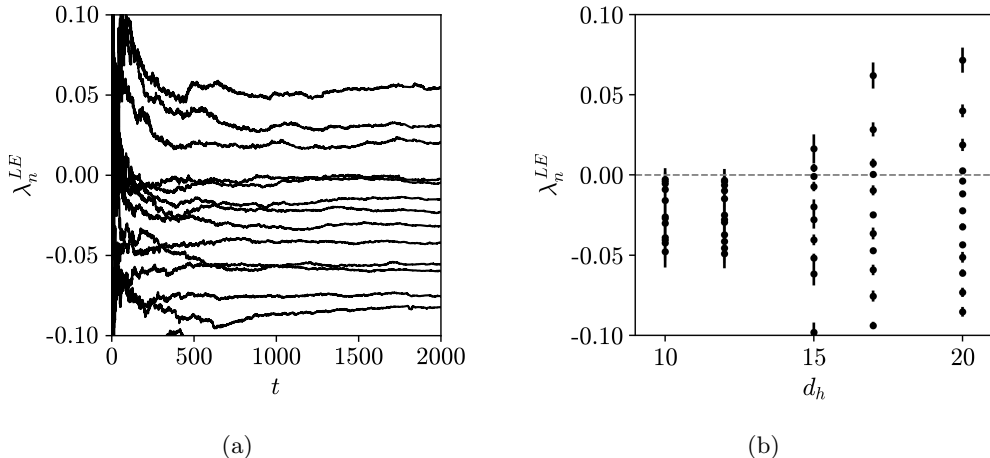


Figure 10: (a) Lyapunov exponents for the DManD models for a single trial at $d_h = 20$. (b) Lyapunov exponents for the DManD models at various dimensions with error bars representing the results from five different trials. The grey dashed line identifies $\lambda_n^{LE} = 0$.

for the manifold, but rather identifying the minimum dimension needed to produce accurate models. Similar results have been observed for plane MFU Couette flow (Linot & Graham 2023; Constante-Amores *et al.* 2024a) and Kolmogorov flow (Pérez-De-Jesús & Graham 2023).

Finally, we examine the leading Lyapunov exponents of the DManD models depending on the dimension of the manifold. Figure 10a displays the spectrum of Lyapunov exponents λ_n^{LE} for the DManD model with $d_h = 20$ through time for a single initial condition. The methods used are those described in Sandri (1996), with the code made available by Rozbeda (2017). We ran the code for over 2000 time units to ensure convergence of the Lyapunov exponents. It is important to note that there is no available information on Lyapunov exponents for the DNS, so we cannot directly compare the DManD model predictions with DNS data. We effectively see three positive exponents, we also observe two exponents near zero due to the spatial translational symmetries in θ and z . Figure 10b displays the exponents, averaged over five different initial conditions, as we vary the dimension of the DManD model. Increasing the model dimension leads to enhancements in the estimation of these Lyapunov exponents. At low dimensions, we do not observe any positive Lyapunov exponents (i.e., models land in a fixed point). We note that we do not observe convergence on the Lyapunov exponents as the dimension increases.

3.4. Finding ECS in the model and DNS

In this section, we leverage the DManD model with a dimension of $d_h = 20$ to explore the state-space of the low-dimensional representation and discover new ECS in the DNS. The primary goal is to use DManD to identify optimal initial conditions, that can be fed into Openpipeflow, which is equipped with an ECS solver for the full-state space. It is essential to highlight that discovering suitable initial conditions is pivotal to guarantee the efficacy of any ECS solver for high-dimensional systems (as we described in the introduction).

First, we summarise the approach that we use to find ECS within the context of DManD. This method follows the framework outlined by Cvitanovic *et al.* (2005), and has been previously used by Linot & Graham (2023). To identify ECS in the full state-space

(which, despite being high-dimensional due to the numerical discretization of the infinite-dimensional NSE, is still finite), our objective is to find an initial condition that leads to a trajectory repeating over a defined time interval T . Thus, we aim to search for solutions where the trajectory's behavior is periodic, essentially involving the identification of zeros in

$$\mathbf{F}(\mathbf{v}, T) = \mathbf{F}_T(\mathbf{v}) - \mathbf{v}, \quad (3.18)$$

here, $\mathbf{F}_T(\mathbf{v})$ refers to the flow map T time units from \mathbf{v} (i.e., $\mathbf{F}_T(\mathbf{v}(t)) = \mathbf{v}(t+T)$). In manifold coordinates, this equation is expressed as

$$\mathbf{H}(\mathbf{h}, T) = \mathbf{G}_T(\mathbf{h}) - \mathbf{h}, \quad (3.19)$$

here, $\mathbf{G}_T(\mathbf{h})$ is the flow map T time units from \mathbf{h} (i.e., $\mathbf{G}_T(\mathbf{h}(t)) = \mathbf{h}(t+T)$). To compute, \mathbf{G}_T , we use equation 2.8. Solving equation 3.19 requires finding both a point \mathbf{h}^* on the periodic orbit and the period T^* , such as $\mathbf{H}(\mathbf{h}^*, T^*) = 0$. We use a Newton-Raphson method to determine \mathbf{h}^* and T^* .

By taking a Taylor series expansion of \mathbf{H} , we find that near the fixed point \mathbf{h}^* , T^* of \mathbf{H} , such that

$$\left. \begin{aligned} \mathbf{H}(\mathbf{h}^*, T^*) - \mathbf{H}(\mathbf{h}, T) &\approx \mathbf{D}_h \mathbf{H}(\mathbf{h}, T) \Delta \mathbf{h} + \mathbf{D}_T \mathbf{H}(\mathbf{h}, T) \Delta T, \\ \mathbf{H}(\mathbf{h}, T) &\approx \mathbf{D}_h \mathbf{H}(\mathbf{h}, T) \Delta \mathbf{h} + \mathbf{g}(\mathbf{G}_T(\mathbf{h})) \Delta T \end{aligned} \right\}$$

where \mathbf{D}_h and \mathbf{D}_T represent the Jacobians of \mathbf{H} with respect to \mathbf{h} and the period T , respectively. Additionally, $\Delta T = T^* - T$ and $\Delta \mathbf{h} = \mathbf{h}^* - \mathbf{h}$. We impose the constraint that the updates of $\Delta \mathbf{h}$ are orthogonal to the vector field \mathbf{h} (i.e., $\mathbf{g}(\mathbf{h})^T \Delta \mathbf{h} = 0$). At a Newton step (i), the system of equations becomes:

$$\begin{bmatrix} \mathbf{D}_h \mathbf{H}(\mathbf{h}^{(i)}, T^{(i)}) & \mathbf{g}(\mathbf{G}_{T^{(i)}}(\mathbf{h}^{(i)})) \\ \mathbf{g}(\mathbf{h}^{(i)})^T & 0 \end{bmatrix} \begin{bmatrix} \Delta \mathbf{h}^{(i)} \\ \Delta T^{(i)} \end{bmatrix} = - \begin{bmatrix} \mathbf{H}(\mathbf{h}^{(i)}, T^{(i)}) \\ 0 \end{bmatrix}, \quad (3.20)$$

here, the standard Newton-Raphson method updates the guesses $\mathbf{h}^{(i+1)} = \mathbf{h}^{(i)} + \Delta \mathbf{h}^{(i)}$ and $T^{(i+1)} = T^{(i)} + \Delta T^{(i)}$.

A Newton scheme can be used to find ECS within high-dimensional data, the computational challenge posed by the Jacobian calculations has prompted the development of various solutions (Page & Kerswell 2020; Page *et al.* 2021; Linot & Graham 2023; Parker & Schneider 2022). Openpipeflow addresses this issue by using a Jacobian-Free Newton-Krylov solver with a Hookstep-trust-region approach, as detailed by Willis (2019). This solver efficiently bypasses the need for explicitly calculating the Jacobian when evaluating the objective function \mathbf{F} . For the exploration of long orbits in pipe flow, Budanur *et al.* (2017) introduced a multiple-shooting method that is successful to identifying relative periodic orbits with periods up to $T \approx 68$. For a more detailed understanding of the ECS solver in the Openpipe flow solver, readers are referred to appendix A of Budanur *et al.* (2017) and Willis *et al.* (2013). The advantage of constructing a low-dimensional model that accurately captures dynamics becomes pivotal in the search for new ECS, as demonstrated in this section. Leveraging the inherent low dimensionality of DMand models, we choose to compute the Jacobian $\mathbf{D}_h \mathbf{H}(\mathbf{h}, T)$ directly using the automatic differentiation tools employed during the training of the NODE. To find these ECS, we use the SciPy ‘hybr’ method, based on a modification of the Powell hybrid method by Virtanen (2020).

Our approach involves randomly selecting 100 initial conditions and exploring five distinct periods $T = [5, 20, 40, 90, 100]$. ECS in the low-dimensional representation that have (nearly) converged are then mapped back to the full space. The criterion for mapping the ECS from the low-dimensional model is a Newton scheme residual of 10^{-2} . While this

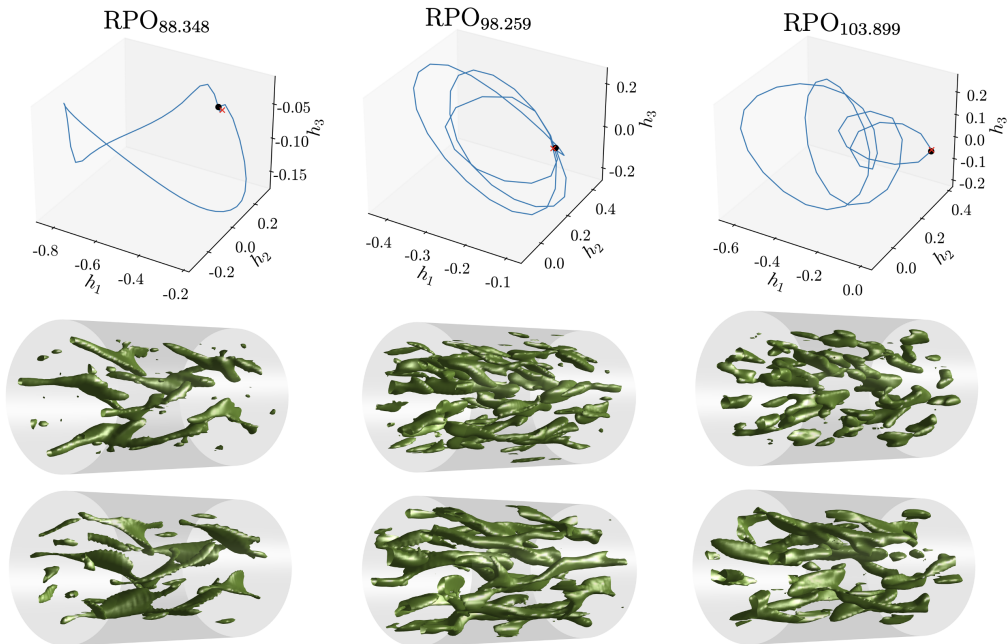


Figure 11: The top panels show the converged ECS by DManD (under certain tolerance) projected onto the first three manifold coordinates that would be used in Openpipeflow. The black dot and red diamond indicate the starting and ending points of the trajectory, respectively. The middle and bottom panels show snapshots of the vorticity flow field using the lambda-2 criterion with a threshold of $\lambda_2 = 0.1$. The middle panels represent the (nearly converged) ECS from the DManD search, while the bottom panels display the converged state from the ECS solver of Openpipeflow. It is noted that for representation purposes, we display $m_p = 1$ instead of $m_p = 4$.

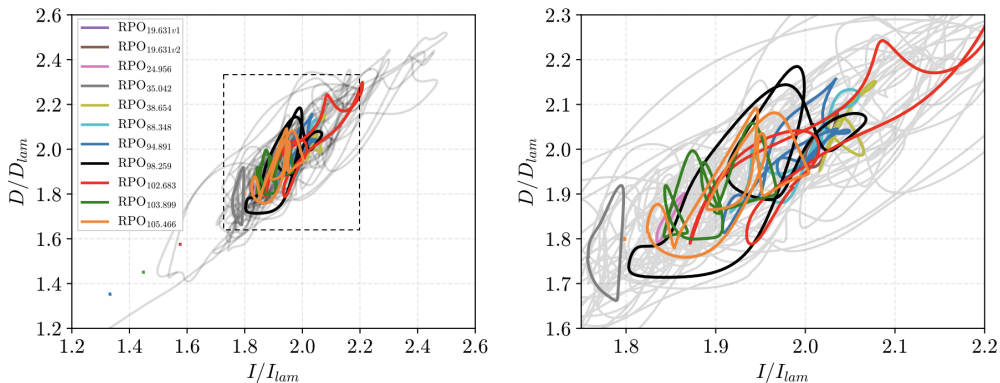


Figure 12: The normalized dissipation versus power input for the collection of invariant solutions displayed in Table 2 with a long trajectory of the DNS turbulence plotted in the background. The dashed box in the left panel outlines the region that is magnified in the right panel for a closer view.

Solution	\bar{D}	\bar{c}	μ^{max}
TW _{1.332}	1.3325	0.93571	0.04056
TW _{1.798}	1.7985	1.6619	0.08803
TW _{1.448}	1.4484	1.8009	0.04892
TW _{1.575}	1.5759	2.7052	0.12259
RPO _{4.891}	1.4740	2.7430	0.06686
RPO _{19.631}	2.0324	3.30392	0.03060
RPO _{19.631}	2.0172	3.30392	0.03605
RPO _{24.956}	1.8644	2.4739	0.03784
RPO _{35.042}	1.7582	1.6211	0.04585
RPO _{36.157}	1.7503	1.8426	0.03465
RPO _{38.654}	2.0475	1.142	0.04499
RPO _{88.348}	1.7985	0.83400	0.04039
RPO _{94.891}	1.9147	4.01616	0.03011
RPO _{98.259}	2.0036	1.5157	0.02991
RPO _{102.683}	1.9793	0.98244	0.02988
RPO _{103.899}	1.9036	6.1943	0.01088
RPO _{105.466}	1.8270	3.0258	0.01653

Table 2: List of new invariant solutions for pipe flow at $Re = 2500$ using initial conditions from the DManD model. The travelling waves are labelled with their dissipation rate \bar{D} , whereas the RPO are labelled by their period T . For each solution, we report the average rate of dissipation \bar{D} , average downstream velocity \bar{c} , and the real part of the largest stability eigenvalue/Floquet exponent μ^{max} .

residual may not be small enough for precise solutions, it provides a good initial guess for the DNS. These initial conditions are subsequently used in Openpipeflow, employing its Newton solver for 100 iterations. It is important to note that the residual of the Newton scheme is reported, providing insights into the convergence behavior of the solver (we highlight that the success criterion for longer orbits is approximately 10^{-4} , as used in previous works such as Willis *et al.* (2013)).

As an illustrative example, the top panels of figure 11 depict the trajectories of three relative periodic orbit discovered by DManD, projected onto the three leading manifold coordinates (h_1, h_2, h_3) . The starting and ending points of the trajectory are denoted by a dot and a diamond, respectively. We remark again that these ‘discovered’ ECS (under certain tolerance) are good initial conditions for the ECS solver in Openpipeflow. We also display the associated vorticity fields by displaying the λ_2 criterion (Jeong & Hussain 1995) for the state of the (nearly) converged ECS from DManD and the converged ECS in Openpipeflow. There is a notable qualitative agreement between these solutions, underscoring the effectiveness of using (nearly) converged solutions from DManD as robust initial conditions for the DNS ECS solver.

Table 2 presents 17 new ECS of pipe flow identified via the ECS solver embedded in Openpipeflow using the (nearly) converged solutions obtained via DManD. RPOs are labeled by their periods T (in units of D/U), while travelling waves (TWs) are labeled by their average dissipation rate (\bar{D}). Additionally, Table 2 includes information regarding the linear stability of each ECS, described by its Floquet multipliers $\Lambda = \exp(\mu_j T + i\theta_j)$. Some of these RPOs are characterized by the longest reported T under these conditions, based on our current knowledge. We note that the DManD solver demonstrates its capability to accurately capture the orbit lengths of the ECS, with errors in their periods

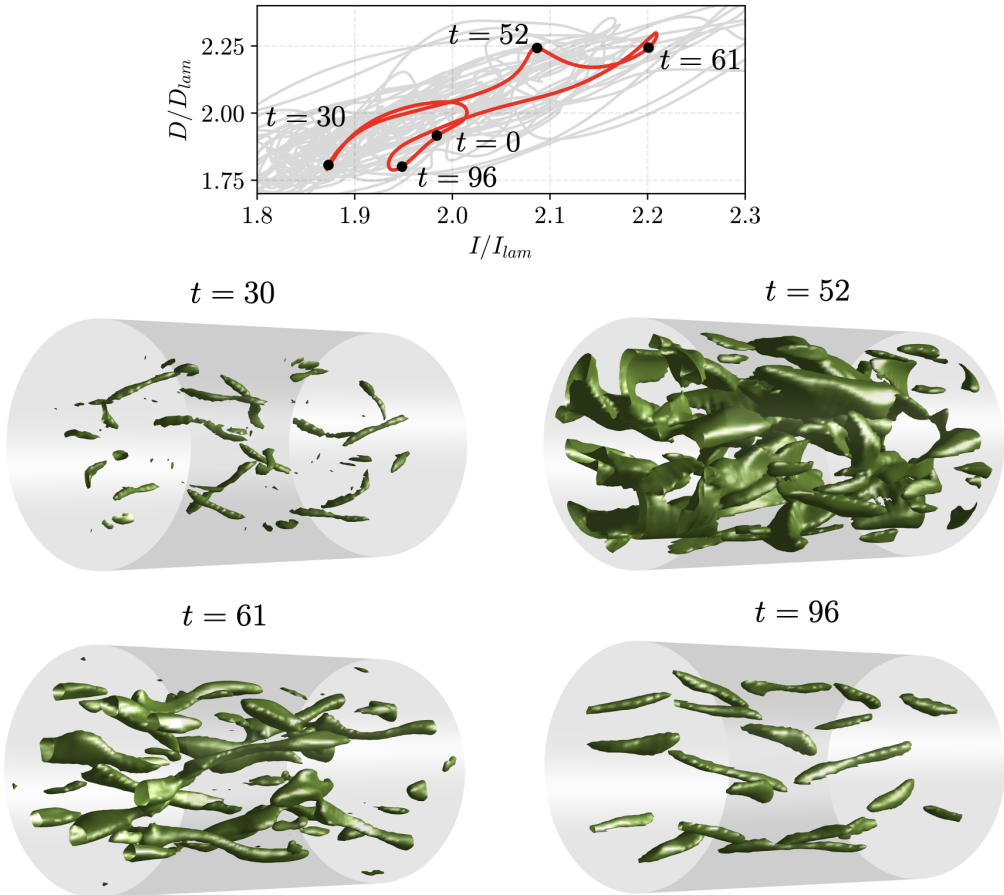


Figure 13: The normalized dissipation versus power input plot for $RPO_{102.683}$ is depicted, with a long trajectory of the DNS turbulence plotted in the background. The black dot points denote the times along the orbit at which 3D snapshots are shown below. Each snapshot displays the lambda-2 criterion with a threshold $\lambda_2 = 0.1$. It is noted that for representation purposes, we display $m_p = 1$ instead of $m_p = 4$.

consistently below 1%. In the remainder of the paper, we focus on representing the orbits from the ECS identified in the DNS solver.

One useful method for visualizing these new invariant solutions is by projecting them onto the dissipation versus energy input plane. Figure 12 illustrates the ID projection of these new ECS, with the darkest shading representing the DNS turbulent attractor. It is expected that turbulence should explore more of the phase space and visit simple invariant solutions, then these ECS should live in the core of the turbulent attractor. This finding is consistent with previous assertions suggesting that the turbulent attractor is guided by ECS Budanur *et al.* (2017). The condition $D = I$ signifies dissipation balancing out energy input, which is the essential requirement for any equilibria or traveling wave (essentially an equilibrium in a co-moving frame of reference). We observe the discovery of four TWs. The darkest region shows that DNS predominantly stays within the region of $1.6 < D/D_{lam} < 2.2$ and $1.7 < I/I_{lam} < 2.2$. Most of the discovered ECS remain

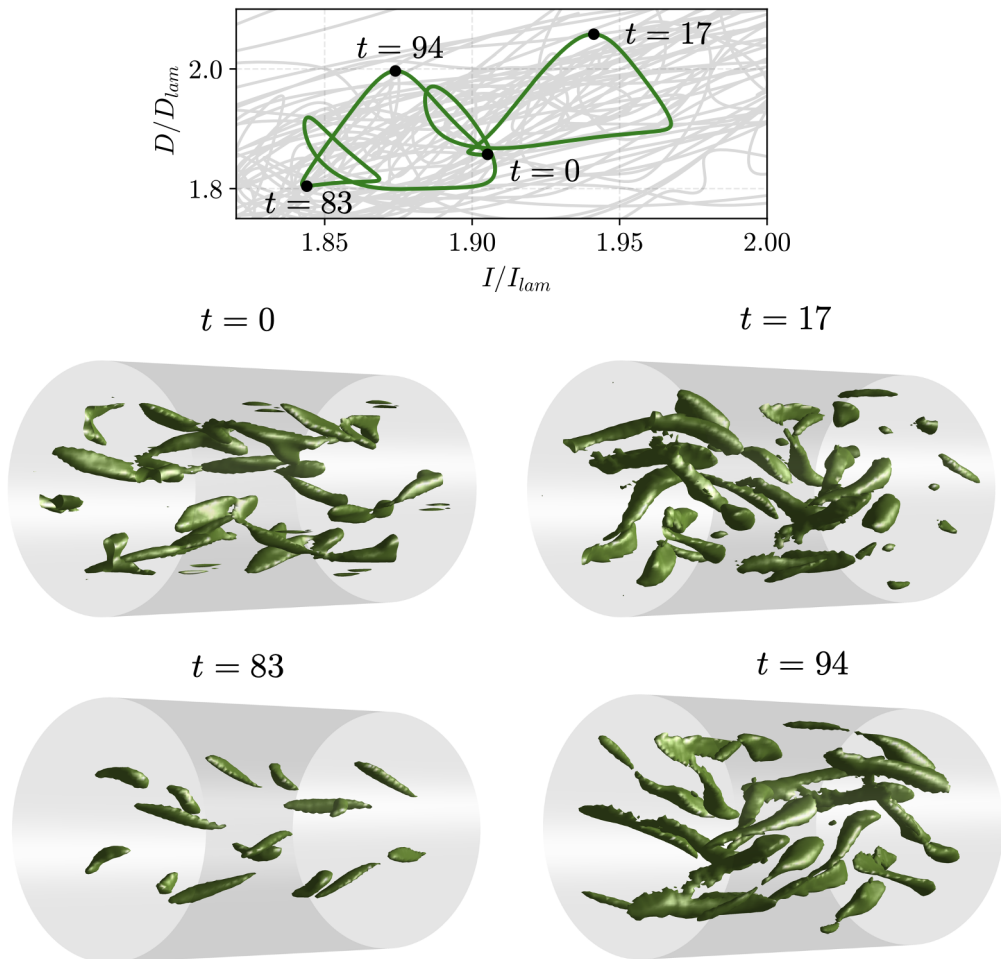


Figure 14: The normalized dissipation versus power input plot for $RPO_{103.899}$ is depicted, with a long trajectory of the DNS turbulence plotted in the background. The black dot points denote the times along the orbit at which 3D snapshots are shown below. Each snapshot displays the lambda-2 criterion with a threshold $\lambda_2 = 0.15$. It is noted that for representation purposes, we display $m_p = 1$ instead of $m_p = 4$.

within this region. In the right panel of figure 12, we present a magnified view 12. This image reveals that many of these RPOs have complex ID curves, whereas the periodic orbits exhibit simple loops.

In Figure 13 and 14, we focus on elucidating the state space of $RPO_{102.683}$ and $RPO_{103.899}$, respectively. The selection of $RPO_{102.683}$ is based on its characteristic complex ID curve, which spans both high and low dissipation regions within the state space. To understand the flow dynamics associated with this RPO, we analyse the vorticity fields by displaying the λ_2 criterion (Jeong & Hussain 1995). At the points of higher dissipation ($t = 52$) and ($t = 61$), the vorticity appears to undergo significant shearing, leading to vortex breakup. High rates of dissipation correspond to intense velocity gradients, and subsequently it leads to high values of the strain rate tensor. This indicates that these

times are characterized by strong and turbulent flow structures. At the lowest point of dissipation, see $t = 30$ and $t = 61$, the vortex structures are much weaker and less pronounced. This weakening of the vortex structures correlates with lower dissipation rates. Then, the dynamics stabilises due to the increases of the power input ($t = 96$), in comparison to $t = 52$. It is worth noting that for these 3D snapshots visualizing just one-eighth of the pipe would suffice due to the shift-and-reflect symmetry (equation 3.3). We have also made available a video of the λ_2 criterion for this case in the supplementary material. Finally, we turn attention to the RPO_{103.899}, figure 14a presents the the ID projection for this RPO, which intriguingly resembles the shadow of two shorter orbits, similar to the described by Budanur *et al.* (2017). This results that the dynamics at the highest point of dissipation at $t = 17$ and $t = 94$ the dynamics exhibit significant shearing, leading to intense vortex interactions and high dissipation rates. These moments are characterized by extreme shearing events. Conversely, at the lowest point of dissipation, for example $t = 83$, the vortex structures are notably weaker. This reduced dissipation corresponds to a more stable and less turbulent flow state.

4. Conclusions

In this study, we have built data-driven models for pressure-driven fluid flow through a circular pipe. To reduce the computational requirements, we impose the shift-and-reflect symmetry to study the system in a minimal computational cell at $Re = 2500$. Nonetheless, this computational size is capable of maintaining the chaotic nonlinear dynamics of turbulence. To build these data-driven models, we employed DManD (Data-driven Manifold Dynamics), an invariant-manifold-based method. DManD is based on the idea of modelling of turbulence from a dynamical systems approach in which the long time dynamics of the dissipative NSE are expected to live in a finite-dimensional invariant manifold. Thus, DManD allows the parameterizing of the invariant manifold with fewer degrees of freedom compared to the original data dimensionality. For learning these manifold coordinates, we first perform a linear dimension reduction with POD, and then a nonlinear dimension reduction via advanced autoencoders which are capable of prediction accurately the low POD coefficients. Finally, we use a state-space approach with Neural ODEs (NODEs) within these learned coordinates to model the dynamics. This combination of linear and nonlinear techniques allows for a compact and efficient representation of the turbulent flow dynamics. Our framework, solely driven by data, enables us to construct models with fewer than 20 degrees of freedom, a significant reduction compared to fully resolved DNS that require on the order of $\mathcal{O}(10^5)$. We note that our claim is not related to the dimensional of the manifold, but to the fact that only 20 degrees of freedom are needed to effectively capture crucial features of the flow, including streak breakdown and the regeneration cycle. In short-time tracking, they accurately track the true trajectory for one Lyapunov time. In the long term, the models successfully capture key aspects of the nonlinear dynamics such as Reynolds stresses and the energy balance.

We have also identified seventeen previously unknown ECS for turbulent pipe flow at $Re = 2500$. The success in discovering these new ECS lies in using (nearly) converged ECS from DManD at $d_h = 20$ as effective initial conditions for the ECS solver in Openpipeflow. To the best of our knowledge, this approach has led to the reporting of RPOs with the longest periods observed for three-dimensional turbulent pipe flow to date. These periodic orbits are situated within the core of the state space traversed by the turbulent attractor. This finding is consistent with previous assertions suggesting that the turbulent attractor is guided by ECS Budanur *et al.* (2017); Page *et al.* (2024).

We acknowledge that accurately modeling turbulent dynamics with significantly fewer degrees of freedom than required for DNS, as demonstrated by the manifold dynamics models presented here, opens up exciting possibilities for dynamical-systems type analyses. These models enable the calculation of local Lyapunov exponents in a computationally efficient manner. We also highlight that we have presented a global description of the manifold, but it would be possible to divide the global manifold topology into many local representations called charts (Floryan & Graham 2022; Fox *et al.* 2023). Finally, data-driven manifold-invariant models facilitate the application of control strategies with minimal degrees of freedom, as exemplified by the use of reinforcement learning techniques in controlling plane MFU Couette flow Linot *et al.* (2023*b*).

Importantly, the models developed in this study are dependent on specific system parameters such as the Reynolds number. Therefore, when transitioning to different Reynolds numbers, it is necessary to obtain a new dataset to adjust the weights of the neural networks for the autoencoders and NODE. Therefore, a crucial direction for future research is to develop models that are less sensitive to specific parameters. The goal is to create robust low-dimensional models capable of transferring knowledge across different parameter regimes. Achieving this would enable broader applications and provide deeper insights into turbulent flow dynamics. This represents a key direction for future research in this field.

Declaration of Interests. The authors report no conflict of interest.

We wish to thank A.P. Willis for making the ‘Openpipeflow’ code open source, and his help to setup the simulations. We gratefully acknowledge Jake Buzhardt for helpful discussions. This work was supported by ONR N00014-18-1-2865 (Vannevar Bush Faculty Fellowship).

REFERENCES

- ABDI, H. & WILLIAMS, L. J. 2010 Principal component analysis. *Wiley interdisciplinary reviews: computational statistics* **2** (4), 433–459.
- AHN, J., LEE, J. H., LEE, J., KANG, J. & SUNG, H. J. 2015 Direct numerical simulation of a 30r long turbulent pipe flow at $re_\tau = 3008$. *Phys. Fluids* **27** (6), 065110.
- AVILA, M., BARKLEY, D. & HOF, B. 2023 Transition to turbulence in pipe flow. *Annu. Rev. Fluid Mech.* **55** (1), 575–602.
- BUDANUR, N. B., SHORT, K. Y., FARAZMAND, M., WILLIS, A. P. & CVITANOVIĆ, P. 2017 Relative periodic orbits form the backbone of turbulent pipe flow. *J. Fluid Mech.* **833**, 274–301.
- CHEN, R. T. Q., RUBANOVA, Y., BETTENCOURT, J. & DUVENAUD, D. 2019 Neural ordinary differential equations. *arXiv:1806.07366*.
- CONSTANTE-AMORES, C., RICARDO, FOX, ANDREW J., JESÚS, CARLOS E. PÉREZ DE & GRAHAM, MICHAEL D. 2024*a* Data-driven Koopman operator predictions of turbulent dynamics in models of shear flows, arXiv: 2407.16542.
- CONSTANTE-AMORES, C. R. & GRAHAM, M. D. 2024 Data-driven state-space and Koopman operator models of coherent state dynamics on invariant manifolds. *J. Fluid Mech.* **984**, R9.
- CONSTANTE-AMORES, C. R., LINOT, A. J. & GRAHAM, M. D. 2024*b* Enhancing predictive capabilities in data-driven dynamical modeling with automatic differentiation: Koopman and neural ODE approaches. *Chaos* **34** (4), 043119.
- CVITANOVIC, P., ARTUSO, R., MAINIERI, R., TANNER, G., VATTAY, G., WHELAN, N. & WIRZBA, A. 2005 Chaos: classical and quantum. *ChaosBook.org (Niels Bohr Institute, Copenhagen 2005)* **69**, 25.

- DARBYSHIRE, A. G. & MULLIN, T. 1995 Transition to turbulence in constant-mass-flux pipe flow. *J. Fluid Mech.* **289**, 83–114.
- DUGGLEBY, A., BALL, K. S., PAUL, M. R. & FISCHER, P. F. 2007 Dynamical eigenfunction decomposition of turbulent pipe flow. *J. Turbul.* **8**, N43.
- DUGUET, Y., WILLIS, A. P. & KERSWELL, R. R. 2008 Transition in pipe flow: the saddle structure on the boundary of turbulence. *J. Fluid Mech.* **613**, 255–274.
- ECKHARDT, B. 2007 Turbulence transition in pipe flow: some open questions. *Nonlinearity* **21** (1), T1.
- ECKHARDT, B., SCHNEIDER, T. M., HOF, B. & WESTERWEEL, J. 2007 Turbulence transition in pipe flow. *Annu. Rev. Fluid Mech.* **39** (1), 447–468.
- EGGELS, J. G. M., UNGER, F., WEISS, M. H., WESTERWEEL, J., ADRIAN, R. J., FRIEDRICH, R. & NIEUWSTADT, F. T. M. 1994 Fully developed turbulent pipe flow: a comparison between direct numerical simulation and experiment. *J. Fluid Mech.* **268**, 175–210.
- EL KHOURY, G. K., SCHLATTER, P., NOORANI, A., FISCHER, P. F., BRETHOUWER, G. & JOHANSSON, A. V 2013 Direct numerical simulation of turbulent pipe flow at moderately high Reynolds numbers. *Flow Turbul Combust* **91**, 475–495.
- FAISST, H. & ECKHARDT, B. 2003 Traveling waves in pipe flow. *Phys. Rev. Lett.* **91**, 224502.
- FAISST, H. & ECKHARDT, B. 2004 Sensitive dependence on initial conditions in transition to turbulence in pipe flow. *J. Fluid Mech.* **504**, 343–352.
- FLORYAN, D. & GRAHAM, M. 2022 Data-driven discovery of intrinsic dynamics. *Nat. Mach. Intell* **4** (12), 1113–1120.
- FOIAS, C., MANLEY, O. & TEMAM, R. 1988 Modelling of the interaction of small and large eddies in two dimensional turbulent flows. *ESAIM: M2AN* **22** (1), 93–118.
- FOX, A. J., R. CONSTANTE-AMORES, C. & GRAHAM, M. D. 2023 Predicting extreme events in a data-driven model of turbulent shear flow using an atlas of charts. *Phys. Rev. Fluids* **8**, 094401.
- GIBSON, JOHN FRANCIS 2002 Dynamical systems models of wall-bounded, shear-flow turbulence. PhD thesis, Cornell University.
- GRAHAM, M D. & FLORYAN, D. 2021 Exact coherent states and the nonlinear dynamics of wall-bounded turbulent flows. *Annu. Rev. Fluid Mech.* **53** (1), 227–253.
- HAMILTON, J. M., KIM, J. & WALEFFE, F. 1995 Regeneration mechanisms of near-wall turbulence structures. *J. Fluid Mech.* **287**, 317–348.
- HELLSTRÖM, L. H. O., MARUSIC, I. & SMITS, A. J. 2016 Self-similarity of the large-scale motions in turbulent pipe flow. *J. Fluid Mech.* **792**, R1.
- HELLSTRÖM, L. H. O. & SMITS, A. J. 2014 The energetic motions in turbulent pipe flow. *Phys. Fluids* **26** (12), 125102.
- HINTON, G. E. & SALAKHUTDINOV, R. R. 2006 Reducing the dimensionality of data with neural networks. *Science* **313** (5786), 504–507.
- HOF, B., VAN DOORNE, C. W. H., WESTERWEEL, J., NIEUWSTADT, F. T. M., FAISST, H., ECKHARDT, B., WEDIN, H., KERSWELL, R. R. & WALEFFE, F. 2004 Experimental observation of nonlinear traveling waves in turbulent pipe flow. *Science* **305** (5690), 1594–1598.
- HOLMES, P., LUMLEY, J. L., BERKOOZ, G. & ROWLEY, C. W. 2012 *Turbulence, Coherent Structures, Dynamical Systems and Symmetry*, 2nd edn. *Cambridge Monographs on Mechanics*. Cambridge University Press.
- HOPF, E. 1948 A mathematical example displaying features of turbulence. *Commun. pure appl. math* **1** (4), 303–322.
- JEONG, J. & HUSSAIN, F. 1995 On the identification of a vortex. *J. Fluid Mech.* **285**, 69–94.
- JIMÉNEZ, J. & MOIN, P. 1991 The minimal flow unit in near-wall turbulence. *J. Fluid Mech.* **225**, 213–240.
- JIMÉNEZ, K. 2013 Near-wall turbulence. *Phys. Fluids* **25** (10), 101302.
- JING, L., ZBONTAR, J. & OTHERS 2020 Implicit rank-minimizing autoencoder. *Advances in Neural Information Processing Systems* **33**, 14736–14746.
- JOLLIFFE, I. T. 1986 *Principal Component Analysis and Factor Analysis*, pp. 115–128. New York, NY: Springer New York.
- KASZÁS, B., CENEDESE, M. & HALLER, G. 2022 Dynamics-based machine learning of transitions in Couette flow. *Phys. Rev. Fluids* **7**, L082402.

- KASZÁS, B. & HALLER, G. 2024 Capturing the edge of chaos as a spectral submanifold in pipe flows. *J. Fluid Mech.* **979**, A48.
- KAWAHARA, G. & KIDA, S. 2001 Periodic motion embedded in plane Couette turbulence: regeneration cycle and burst. *J. Fluid Mech.* **449**, 291–300.
- KAWAHARA, G., UHLMANN, M. & VAN VEEN, L. 2012 The significance of simple invariant solutions in turbulent flows. *Annu. Rev. Fluid Mech.* **44** (Volume 44, 2012), 203–225.
- KRAMER, MARK A. 1991 Nonlinear principal component analysis using autoassociative neural networks. *AIChE Journal* **37** (2), 233–243.
- LEE, M. & MOSER, R. D. 2015 Direct numerical simulation of turbulent channel flow up to $Re_\tau \approx 5200$. *J. Fluid Mech.* **774**, 395–415.
- LI, M., JAIN, S. & HALLER, G. 2022 Nonlinear analysis of forced mechanical systems with internal resonance using spectral submanifolds, part i: Periodic response and forced response curve. *Nonlinear Dynamics* **110** (2), 1005–1043.
- LINOT, A. J., BURBY, J. W., TANG, Q., BALAPRAKASH, P., GRAHAM, M. D. & MAULIK, R. 2023a Stabilized neural ordinary differential equations for long-time forecasting of dynamical systems. *J. Comput. Phys.* **474**, 111838.
- LINOT, A. J. & GRAHAM, M. D. 2020 Deep learning to discover and predict dynamics on an inertial manifold. *Phys. Rev. E* **101**, 062209.
- LINOT, A. J. & GRAHAM, M. D. 2022 Data-driven reduced-order modeling of spatiotemporal chaos with neural ordinary differential equations. *Chaos* **32** (7), 073110.
- LINOT, A. J. & GRAHAM, M. D. 2023 Dynamics of a data-driven low-dimensional model of turbulent minimal Couette flow. *J. Fluid Mech.* **973**, A42.
- LINOT, A. J., ZENG, K. & GRAHAM, M. D. 2023b Turbulence control in plane Couette flow using low-dimensional neural ODE-based models and deep reinforcement learning. *Int J Heat Fluid Flow* **101**, 109139.
- LIU, A., AXÅS, J. & HALLER, G. 2024 Data-driven modeling and forecasting of chaotic dynamics on inertial manifolds constructed as spectral submanifolds. *Chaos* **34** (3), 033140.
- DE LOZAR, A., MELLIBOVSKY, F., AVILA, M. & HOF, B. 2012 Edge state in pipe flow experiments. *Phys. Rev. Lett.* **108**, 214502.
- MILANO, M & KOUMOUTSAKOS, P 2002 Neural network modeling for near wall turbulent flow. *J. Comput. Phys.* **182** (1), 1–26.
- MULLIN, T. 2011 Experimental studies of transition to turbulence in a pipe. *Annu. Rev. Fluid Mech.* **43** (1), 1–24.
- NAGATA, M. 1990 Three-dimensional finite-amplitude solutions in plane Couette flow: bifurcation from infinity. *J. Fluid Mech.* **217**, 519–527.
- OTTO, S. E. & ROWLEY, C. W. 2019 Linearly recurrent autoencoder networks for learning dynamics. *SIAM J. Appl. Dyn. Syst* **18** (1), 558–593.
- PAGE, J, BRENNER, M P. & KERSWELL, R R. 2021 Revealing the state space of turbulence using machine learning. *Phys. Rev. Fluids* **6**, 034402.
- PAGE, J. & KERSWELL, R. R. 2019 Koopman mode expansions between simple invariant solutions. *J. Fluid Mech.* **879**, 1–27.
- PAGE, J. & KERSWELL, R. R. 2020 Searching turbulence for periodic orbits with dynamic mode decomposition. *J. Fluid Mech.* **886**, A28.
- PAGE, J, NORGAARD, P., BRENNER, M. P. & KERSWELL, R. R. 2024 Recurrent flow patterns as a basis for two-dimensional turbulence: Predicting statistics from structures. *PNAS* **121** (23), e2320007121.
- PARKER, J.P. & SCHNEIDER, T.M. 2022 Variational methods for finding periodic orbits in the incompressible navier–stokes equations. *J. Fluid Mech.* **941**, A17.
- PASZKE, A. *et al.* 2019 Pytorch: An imperative style, high-performance deep learning library. In *Advances in Neural Information Processing Systems* (ed. H. Wallach, H. Larochelle, A. Beygelzimer, F. d'Alché-Buc, E. Fox & R. Garnett), , vol. 32. Curran Associates, Inc.
- PATHAK, J., HUNT, B., GIRVAN, M., LU, Z. & OTT, E. 2018 Model-free prediction of large spatiotemporally chaotic systems from data: A reservoir computing approach. *Phys. Rev. Lett.* **120**, 024102.
- PÉREZ-DE-JESÚS, C. E & GRAHAM, M. D. 2023 Data-driven low-dimensional dynamic model of Kolmogorov flow. *Phys. Rev. Fluids* **8**, 044402.

- PIROZZOLI, S. 2024 On the streamwise velocity variance in the near-wall region of turbulent flows. *J. Fluid Mech.* **989**, A5.
- PIROZZOLI, S., ROMERO, J., FATICA, M., VERZICCO, R. & ORLANDI, P. 2021 One-point statistics for turbulent pipe flow up to $re_\tau \approx 6000$. *J. Fluid Mech.* **926**, A28.
- PLATT, J. A., PENNY, S. G., SMITH, T. A., CHEN, T. & ABARBANEL, H. D.I. 2022 A systematic exploration of reservoir computing for forecasting complex spatiotemporal dynamics. *Neural Networks* **153**, 530–552.
- POPE, S. B. 2000 *Turbulent Flows*. Cambridge University Press.
- PRINGLE, C. C.T, DUGUET, Y. & KERSWELL, R. R 2009 Highly symmetric travelling waves in pipe flow. *Philosophical Transactions of the Royal Society A: Mathematical, Physical and Engineering Sciences* **367** (1888), 457–472.
- PRINGLE, C. C. T. & KERSWELL, R. R. 2007 Asymmetric, helical, and mirror-symmetric traveling waves in pipe flow. *Phys. Rev. Lett.* **99**, 074502.
- RACCA, A & MAGRI, L 2022 Data-driven prediction and control of extreme events in a chaotic flow. *Phys. Rev. Fluids* **7**, 104402.
- REYNOLDS, O 1883 An experimental investigation of the circumstances which determine whether the motion of water shall be direct or sinuous, and of the law of resistance in parallel channels. *Philos. Trans. R. Soc. A* **174**, 935–982.
- ROWLEY, C. W., MEZIC, I., BAGHERI, S., SCHLATTER, P & HENNINGSON, D. S. 2009 Spectral analysis of nonlinear flows. *J. Fluid Mech.* **641**, 115–127.
- ROZBEDA, P. 2017 pylyapunov. available at: <https://github.com/paulrozdeba/pylyapunov> .
- SANDRI, M 1996 Numerical calculation of Lyapunov exponents. *Math. J.* **6**.
- SCHMID, P. J. 2010 Dynamic mode decomposition of numerical and experimental data. *J. Fluid Mech.* **656**, 5–28.
- SMITS, A. J., MCKEON, B. J. & MARUSIC, I. 2011 High-Reynolds number wall turbulence. *Annu. Rev. Fluid Mech.* **43** (1), 353–375.
- TEMAM, R. 1989 Do inertial manifolds apply to turbulence? *Phys. D: Nonlinear Phenom.* **37** (1), 146–152.
- VIRTANEN, *et al.* 2020 Scipy 1.0: fundamental algorithms for scientific computing in python. *Nature methods* **17** (3), 261–272.
- VISWANATH, D & CVITANOVIĆ, P 2009 Stable manifolds and the transition to turbulence in pipe flow. *J. Fluid Mech.* **627**, 215–233.
- WALEFFE, F. 1998 Three-dimensional coherent states in plane shear flows. *Phys. Rev. Lett.* **81**, 4140–4143.
- WALEFFE, F. 2001 Exact coherent structures in channel flow. *J. Fluid Mech.* **435**, 93–102.
- WEDIN, H. & KERSWELL, R. R. 2004 Exact coherent structures in pipe flow: travelling wave solutions. *J. Fluid Mech.* **508**, 333–371.
- WILLIS, A. P 2017 The openpipeflow Navier-Stokes solver. *SoftwareX* **6**, 124–127.
- WILLIS, A. P. 2019 Equilibria, periodic orbits and computing them, arXiv: 1908.06730.
- WILLIS, A. P., CVITANOVIĆ, P. & AVILA, M. 2013 Revealing the state space of turbulent pipe flow by symmetry reduction. *J. Fluid Mech.* **721**, 514–540.
- WILLIS, A. P. & KERSWELL, R. R. 2008 Coherent structures in localized and global pipe turbulence. *Phys. Rev. Lett.* **100**, 124501.
- WILLIS, A. P. & KERSWELL, R. R. 2009 Turbulent dynamics of pipe flow captured in a reduced model: puff relaminarization and localized ‘edge’ states. *J. Fluid Mech.* **619**, 213–233.
- WILLIS, A. P., SHORT, K. Y. & CVITANOVIĆ, P. 2016 Symmetry reduction in high dimensions, illustrated in a turbulent pipe. *Phys. Rev. E* **93**, 022204.
- YOUNG, C. D., CORONA, P. T., DATTA, A., HELGESON, M. E. & GRAHAM, M. D. 2023 Scattering-Informed Microstructure Prediction during Lagrangian Evolution (SIMPLE)—a data-driven framework for modeling complex fluids in flow. *Rheologica Acta* **62** (10), 587–604.
- ZELIK, S. 2022 Attractors: Then and now, arXiv: 2208.12101.
- ZENG, K., PÉREZ-DE-JESÚS, C. E, FOX, A. J & GRAHAM, M. D 2024 Autoencoders for discovering manifold dimension and coordinates in data from complex dynamical systems. *MLST* **5** (2), 025053.